JOURNAL OF GEOPHYSICAL RESEARCH, VOL. 96, NO. B13, PAGES 21,753–21,777, DECEMBER 10, 1991

An Empirical Method for Calculating Melt Compositions Produced Beneath Mid-Ocean Ridges: Application for Axis and Off-Axis (Seamounts) Melting

YAOLING NIU AND RODEY BATIZA

School of Ocean and Earth Sciences and Technology, University of Hawaii at Manoa, Honolulu

We present a new method for calculating the major element compositions of primary melts parental to mid-ocean ridge basalt (MORB). This model is based on the experimental data of Jaques and Green (1980), Falloon et al. (1988), and Falloon and Green (1987, 1988) which are ideal for this purpose. Our method is empirical and employs solid-liquid partition coefficients (D_i) from the experiments. We empirically determine $D_i = f(P,F)$ and use this to calculate melt compositions produced by decompression-induced melting along an adiabat (column melting). Results indicate that most MORBs can be generated by 10–20% partial melting at initial pressures (P_O) of 12–21 kbar. Our primary MORB melts have MgO = 10–12 wt %. We fractionate these at low pressure to an MgO content of 8.0 wt % in order to interpret natural MORB liquids. This model allows us to calculate P_O, P_f, T_O, T_f, and F for natural MORB melts. We apply the model to interpret MORB compositions and mantle upwelling patterns beneath a fast ridge (East Pacific Rise (EPR) 8°N to 14°N), a slow ridge (mid-Atlantic Ridge (MAR) at 26°S), and seamounts near the EPR (Lamont seamount chain). We find mantle temperature differences of up to 50°–60°C over distances of 30–50 km both across axis and along axis at the EPR. We propose that these are due to upward mantle flow in a weakly conductive (versus adiabatic) temperature gradient. We suggest that the EPR is fed by a wide (~100 km) zone of upwelling due to plate separation but has a central core of faster buoyant flow. An along-axis thermal dome between the Siqueiros transform and the 11°45' Overlapping Spreading center (OSC) may represent such an upwelling; however, in general there is a poor correlation between mantle temperature, topography, and the segmentation pattern at the EPR. For the Lamont seamounts we find regular across-axis changes in P_O and F suggesting that the melt zone pinches out off axis. This observation supports the idea that the EPR is fed by a broad upwelling which diminishes in vigor off axis. In contrast with the EPR axis, mantle temperature correlates well with topography at the MAR, and there is less melting under offsets. The data are consistent with weaker upwelling under offsets and an adiabatic temperature gradient in the subaxial mantle away from offsets. The MAR at 26°S exhibits the so-called local trend of Klein and Langmuir (1989). Our model indicates that the local trend cannot be due solely to intracolumn melting processes. The local trend seems to be genetically associated with slow-spreading ridges, and we suggest it is due to melting of multiple individual domains that differ in initial and final melting pressure within segments fed by buoyant focused mantle flow.

Introduction

Several recent studies [*McKenzie*, 1984; *Klein and Langmuir*, 1987; *McKenzie and Bickle*, 1988] have emphasized that melting occurring in adiabatically rising mantle material is polybaric. It is now widely accepted that mid-ocean ridge basalts (MORB) are produced by such melting, commonly referred to as column melting. In this model, solid mantle material rises along an adiabatic temperature gradient, intersects the solidus at a depth determined by its temperature and melting characteristics, and begins to melt. Continued upwelling is accompanied by continuous melting, matrix compaction, and melt segregation.

While this general scenario for the genesis of MORB has gained wide acceptance, many of the details of the process and how these might vary in specific tectonic settings remain controversial. For example, some studies favor a wide (~100 km) zone of passive mantle upwelling resulting from plate separation [e.g., *Oxburgh and Turcotte*, 1968; *Hanks*, 1971; *Bottinga and Allègre*, 1978; *Houseman*, 1983; *Phipps Morgan*, 1987; *Spiegelman and McKenzie*, 1987; *Sleep*, 1988; *Ribe*, 1988]. Alternatively, a narrow (10–20 km) zone of upwelling is favored by models which consider thermal, compositional, and melt buoyancy forces [e.g., *Scott and Stevenson*, 1989; *Sotin and Parmentier*, 1989; *Buck and Su*, 1989] and diapiric flow [*Rabinowicz et al.*, 1987; *Whitehead et al.*, 1984; *Crane*, 1985; *Schouten et al.*, 1985; *Nicolas*, 1986, 1989].

The amount and distribution of melt in the column, the mechanism of melt segregation, and the role of lateral melt migration to focus melt below the very narrow (~1 km) axial neovolcanic zone are also controversial. Theoretical arguments [e.g., *McKenzie*, 1984; *Richter and McKenzie*, 1984; *Ribe*, 1987; *Riley and Kohlstedt*, 1990] suggest that melt porosities in the mantle are likely to be small (1–3 %), but exactly how small is debatable. Even small (1–2%) melt porosity can provide significant buoyancy [*Scott and Stevenson*, 1989; *Niu and Batiza*, 1991]. Recent trace element studies of abyssal peridotites [*Johnson et al.*, 1990] also suggest small melt porosities and favor fractional melting over batch partial melting for MORBs [*Dick*, 1989]. Small melt porosities support the continuous melting model of *Langmuir et al.* [1977], also termed critical melting [*Maaløe*, 1982].

The level and physical mechanisms of melt segregation are also controversial. The maximum depth where dikes may be efficient melt conduits [*Nicolas*, 1986; *Sleep*, 1988] is unknown, but interpretation of uranium decay series isotopes [*Rubin and Macdougall*, 1985; *McKenzie*, 1985*a*; *Williams and Gill*, 1989] shows that MORB melts probably are produced, segregated, and erupted relatively rapidly. This is also favored by the observation that MORB melts do not chemically reequilibrate at shallow depths [*Bedard*, 1989] (T. Plank and C.

Paper number 91JB01933.
0148-0227/91/91JB-01933$05.00

H. Langmuir, Influence of the melting region on mid-ocean ridge basalt chemistry, submitted to Journal of Geophysical Research, 1991) (Hereinafter Plank and Langmuir, 1991). If the zone of upwelling is broad, then lateral melt migration toward the axis may be needed to focus eruptions in the narrow neovolcanic zone [*Phipps Morgan*, 1987; *Scott and Stevenson*, 1989]. However, the importance of this process is presently difficult to evaluate.

Additional unresolved questions concern the manner in which mantle upwelling and magma supply vary with spreading rate of mid-ocean ridges. Several studies [e.g., *Scott and Stevenson*, 1989; *Sotin and Parmentier*, 1989] have suggested that upwelling may be episodic or periodic at slow spreading rates. *Schouten et al.* [1985] suggested a spreading rate dependence of the spacing of central supply conduits feeding ridges. In contrast, others [e.g., *Macdonald et al.*, 1988; *Sinton et al.*, 1991] suggest a hierarchic supply geometry like that proposed by *Langmuir et al.* [1986]. Recently, *Lin and Phipps Morgan* [1991] suggested that fast-spreading ridges may be dominated by spreading-induced passive upwelling, whereas at slow-spreading ridges, buoyant plumes may be more important. The buoyancy could come from melt, large temperature difference, and/or compositional buoyancy created by the melting processes. The significance of ridge offsets in perturbing mantle flow and causing edge effects on MORB chemistry also is a subject of debate [e.g., *Bender et al.*, 1984; *Phipps Morgan and Forsyth*, 1988].

The chemistry of MORB melts provides an important line of evidence for helping to answer these questions and others. The major element chemistry of MORB is particularly helpful when compared to the chemistry of melts produced in the laboratory under controlled conditions. For this reason, there have been several previous attempts to use the experiments to deduce the conditions of melting (e.g., pressure of melting, extent of partial melting, nature of the peridotite source) of natural MORB glasses. *Ito* [1973] used existing experimental data to quantify phase equilibria in the basalt-peridotite system. More recently, *Klein and Langmuir* [1987], *McKenzie and Bickle* [1988], and R. J. Kinzler and T. L. Grove (Primary magmas of mid-ocean ridge basalts, submitted to Journal of Geophysical Research, 1991) (hereinafter Kinzler and Grove, 1991), using different approaches, have attempted to use experimental data to calculate the chemical compositions of MORB melts formed under a variety of melting conditions.

In this paper, we present a method, based on experimental data, for calculating MORB melts formed by decompression-induced melting processes. Our interest is not only to understand the origin of MORB and magmatic processes at ridge axes but also to provide a self-consistent set of MORB melt compositions for use in physical models of upwelling, flow, melt migration, and other physical-chemical processes beneath mid-ocean ridges. Since the chemistry of MORB melts controls their density [*Niu and Batiza*, 1991], viscosity, and other physical properties, chemical information will also be of use as an input to physical models of magmatic and tectonic processes at active ridges. In this paper, we first discuss the experimental data upon which our model is based. We then present the method and discuss its possible applications to interpreting the origin of natural MORB melts. Finally, we apply the method to three MORB suites from a fast ridge (the East Pacific Rise (EPR) at 8°–14°N), a slow ridge (the mid-Atlantic ridge (MAR) at 26°S), and a seamount chain formed near the EPR (the Lamont seamount chain at ~ 10°N). We discuss these results and draw some conclusions regarding magmatic processes occurring below the plate boundary zone.

THE METHOD

Experimental Data

There exist a great deal of experimental data bearing on the origin of MORB melts. These data have been recently reviewed by *Falloon and Green* [1987, 1988], *Elthon* [1989, 1990], and *Fujii* [1989]. In this study, we have relied on the experiments of *Jaques and Green* [1980] and *Falloon et al.* [1988] and also have incorporated some results from *Falloon and Green* [1987, 1988]. These experiments are conducted with several starting compositions and cover a wide range of temperatures and pressures. *Jaques and Green* [1980] conducted isobaric batch melting runs using Hawaiian Pyrolite (HPY) and Tinaquillo Lherzolite (TQL) modified by subtracting 40% olivine ($Fo_{91.6}$ and $Fo_{91.9}$, respectively) to facilitate identification of minor phases. However, iron loss and quench modification hamper obtaining equilibrium partial melt compositions directly. They avoided these problems by analyzing all the residual crystal phases, combined with modal analysis of the entire charge, and obtained calculated equilibrium partial melts (CEPM) by mass balance.

Recently, *Falloon and Green* [1987, 1988] and *Falloon et al.* [1988] showed that the CEPM of *Jaques and Green* [1980] are too olivine-rich. They concluded that the CEPM of *Jaques and Green* [1980] incorporated errors in the modal analysis (especially in distinguishing fine-grained olivine and orthopyroxene) and phase compositions of residual minerals when compositional zoning was present. *Falloon et al.* [1988] also point to problems in the resultant SiO_2 and Al_2O_3 contents of the CEPM. Because of these potential problems, we have carefully compared the *Jaques and Green* [1980] and *Falloon et al.* [1988] data. Plotting these data against each other shows excellent agreement for most elements for both starting compositions (HPY and TQL) as the correlations have slopes of 1.00 ± 0.05 and $R^2 > 0.94$. However, there are indeed some differences in SiO_2 and MgO for both HPY and TQL as well as in Al_2O_3 and FeO for TQL. *Falloon et al.* [1988] carried out reversal and/or sandwich experiments on CEPM of *Jaques and Green* [1980] by using Fe, Pt, and graphite capsules. The gain and loss of iron are inevitable when using Fe and Pt capsules, although the absolute amount is difficult to evaluate. However, the runs using Fe and Pt capsules should roughly bracket the unmodified melt concentrations if equilibrium is approached.

Figure 1 shows the comparison of these data and indicates that the discrepancies between *Jaques and Green* [1980] and *Falloon et al.* [1988] are, in general, systematic. Assuming that the data of *Falloon et al.* [1988] constrained by graphite capsule runs and bracketed by Fe and Pt capsule runs are correct, then the CEPM of *Jaques and Green* [1980] can be corrected for these discrepancies. Figure 1 shows that the differences in SiO_2 are ~0.5 wt % for HPY and ~1 wt % for TQL. The Al_2O_3 contents in three runs of TQL are clearly high, but can be corrected in a straightforward manner. The FeO difference for TQL and the MgO difference for HPY can also be corrected. For MgO of TQL the difference seems to be independent of capsule material. This comparison gives us confidence that the data set of *Jaques and Green* [1980] is in fact of high quality considering experimental difficulties. Thus, in our model we use the data of *Jaques and Green* [1980] and *Falloon et al.*

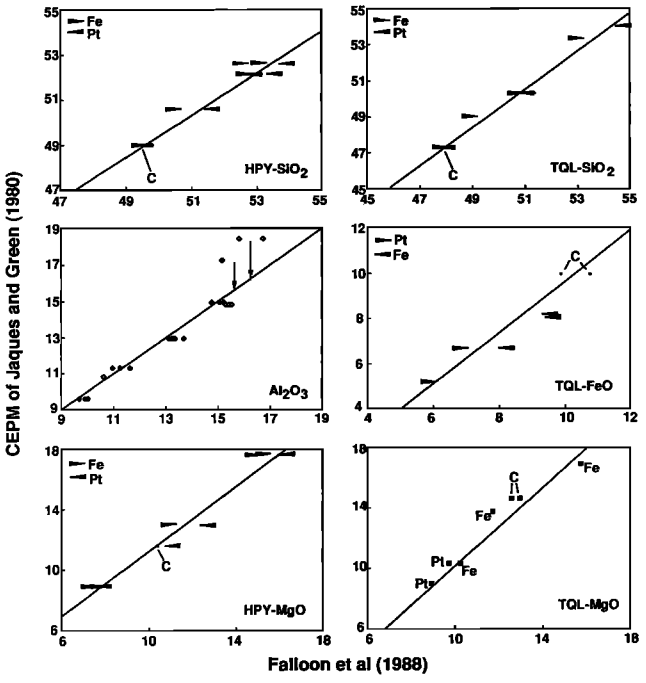

Fig. 1. For most elements, the calculated equilibrium partial melts (CEPM) of *Jaques and Green* [1980] are in excellent agreement with the reversal experiments of *Falloon et al.* [1988]. This figure shows that the discrepancies that do exist are systematic. The experiments of *Falloon et al.* [1988] using Pt, Fe, and graphite (C) capsules can be used to bracket the systematic differences in SiO_2 and FeO for Tinaquillo Lherzolite (TQL) and SiO_2 and MgO for Hawaiian Pyrolite (HPY). The discrepancies in MgO for TQL seem to be independent of capsule materials used. The three runs of *Jaques and Green* [1980] for TQL have obvious high values in Al_2O_3 (open diamonds). Assuming the recent experiments are more reliable, we can correct the CEPM.

[1988] for HPY and TQL plus the data of *Falloon and Green* [1987, 1988] for MORB pyrolite 90, which is a more reasonable source peridotite for MORB than HPY (not depleted enough) or TQL (too depleted).

Determination of Major Oxide Partitioning From Experimental Data

To compute the major element composition of peridotite melts, it would be ideal to use a thermodynamic basis taking account of mineral compositions, modal abundances, reactions occurring during melting, and changes in pressure (P) and temperature (T). For low-pressure conditions, such models have been reasonably successful [e.g., *Langmuir and Hanson*, 1980*b*; *Nielsen and Dungan*, 1983; *Ghiorso and Carmichael*, 1985; *Nielsen*, 1985, 1988; *Weaver and Langmuir*, 1990]. However, there is not yet enough information to confidently employ such models at high pressure. For this reason, our approach here is empirical.

Since the potential complexities attending melting are all reflected in melt composition, we attempt to extract from the experimental data the apparent bulk solid-liquid partition coefficients (D_i) for each oxide component (i):

$$D_i = x_i^s / x_i^l, \tag{1}$$

where x_i^s is the weight percent of component i in the solid and x_i^l is the weight percent of i in the liquid. Using mass balance, we have

$$x_i^o = F x_i^l + (1 - F) x_i^s, \tag{2}$$

where x_i^o is the weight percent of i in the peridotite source and F is the fraction of melt produced. Combining (1) and (2), we thus have

$$D_i \equiv x_i^s / x_i^l = \frac{x_i^o / x_i^l - F}{1 - F}. \tag{3}$$

Equation (3) is used to derive D_i values from the experimental data of *Jaques and Green* [1980] and *Falloon et al.* [1988] of SiO_2, TiO_2, Al_2O_3, FeO, MgO, CaO, Na_2O, and K_2O for HPY and TQL source compositions. Ideally, these derived D_i values and the corresponding experimental run conditions (i.e., P and T) could be used to find an expression $D_i = f(T, P)$ for each source composition. Thermodynamically, this may be expressed in logarithmic form:

$$\ln D_i = c_1/T + c_2 + c_3\, P/T + f(x) \tag{4}$$

where c_1, c_2, and c_3 are constants, P and T are pressure and temperature, and $f(x)$ is a function dealing with the compositions of the solid phases and liquid in the system and probably also depends on pressure and temperature. In practice, however, to find an explicit form for (4) is not possible with available data. Fortunately, using F, the extent of partial melting, as a single variable can substantially simplify the problem. This is because F implicitly contains temperature and compositional information about the melting process. As illustrated in Figure 2, we find that F is linearly related to temperature for each pressure considered by *Jaques and Green* [1980], that is,

$$F(\text{wt\%}) = a + b\, P(\text{kb}) + \{c + d\, P(\text{kb})\} T(^\circ\text{C}), \tag{5}$$

where a, b, c, and d are empirical constants for each of the given source compositions (HPY and TQL). Table 1 gives these coefficients for HPY and TQL and shows that their dependence on bulk composition is not large, as the coefficients for these very different peridotites are within 10% of each other (except for a : 17%). Figure 3 compares

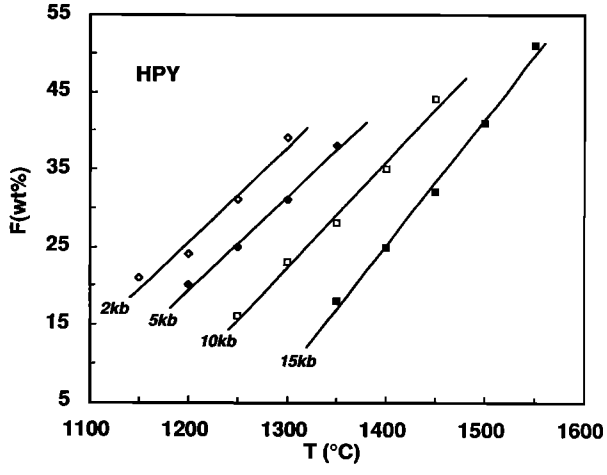

Fig. 2. The extent of partial melting (F, weight percent) versus temperature (T, degrees Celsius) for four pressure values from experiments on HPY of *Jaques and Green* [1980]. F is a linear function of temperature alone at constant pressure for the range of F investigated. At low F (<10%), the relationship between F and T is probably nonlinear.

Table 1. Empirical Coefficients determined for Extent of partial melting

Source	a	b, Kbar^{-1}	c, °C^{-1}	d, Kbar^{-1}•C^{-1}
HPY	- 98.620	- 6.551	0.10872	3.347×10^{-3}
TQL	- 117.149	- 6.028	0.11679	3.023×10^{-3}

$F(wt\%) = a + b\,P(kb) + \{c + d\,P(kb)\}\,T(°C)$.
HPY – Hawaiian pyrolite; TQL – Tinaquillo lherzolite.

experimental values of F with those calculated using (5). It is important to note that (5) is purely empirical and should not be extrapolated outside the range of the experimental data. For example, it cannot be used to derive the solidus because of the lack of experimental data on very low extents of partial melting, and because F increases nonlinearly in the first few tens of degrees above the solidus [*Jaques and Green*, 1980; *McKenzie and Bickle*, 1988]. Figure 4 shows the isopleths of F for HPY and TQL. These are calculated using (5) except for the solidus and dashed isopleths near the solidus, which are from *Jaques and Green* [1980, Figures 1 and 2].

The next step in our model is to empirically derive an expression for $D_i = f(P,T)$. But since at constant pressure, F only depends on T, we instead derive an expression for $D_i = f(P,F)$. Our empirical technique for deriving this expression for each oxide component is illustrated in Figure 5 using SiO_2. This shows D_{SiO_2} as a function of F for several pressures for both HPY and TQL. For the eight oxides we consider, we find

$$D_i = e + f\,F(wt\%) + g\,/F(wt\%) + h\,P(kb) + i\,P/F, \qquad (6)$$

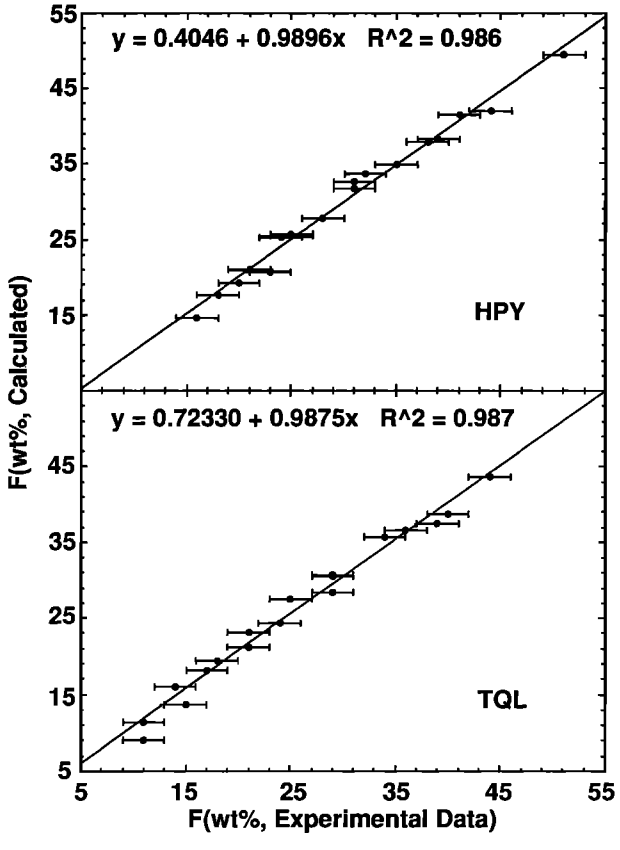

Fig. 3. A comparison of the extent of partial melting (F) determined by *Jaques and Green* [1980] with F calculated using our empirical expression (equation (5)) for both HPY and TQL. The equation is for the regression line.

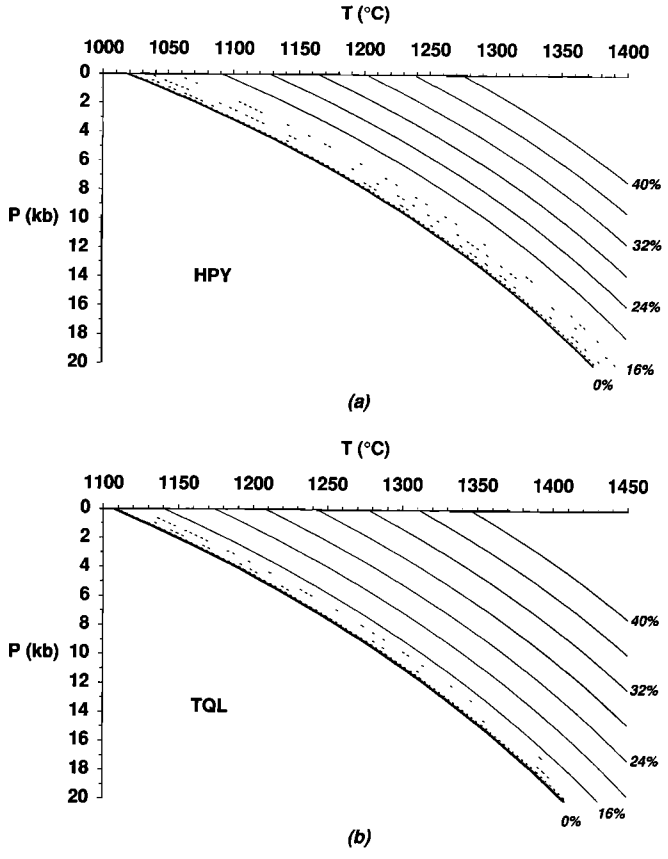

Fig. 4. Calculated extent of partial melting (solid lines) using (5) for (*a*) HPY and (*b*) TQL as a function of temperature (degrees Celsius) and pressure (kilobars). The heavy solid line is the solidus from Figure 1 of *Jaques and Green* [1980]. The dashed isopleths are from Figure 2 of *Jaques and Green* [1980].

where e, f, g, h, and i are empirical coefficients which differ slightly for each bulk composition. Table 2 gives the coefficients for HPY and TQL, and Figure 6 compares calculated D_i values with those derived from the experimental data. In Figure 7 we directly compare the weight percent of each oxide with the CEPM for both starting compositions. This figure also shows that typical uncertainties for calculated D_i values and weight percents are about the same as analytical uncertainties.

Equation (6) and Table 2 quantify the following features of isobaric batch melting found by *Jaques and Green* [1980] and *Falloon and Green* [1987, 1988]. (1) The D_i for all oxides are strongly dependent on F. In some cases, this dependence is linear or nearly linear, but in other cases the dependence is non-linear. (2) The D_i for SiO_2, Al_2O_3, FeO, MgO, and CaO show clear pressure dependence. (3) The behavior of FeO is complex: at low pressure, the FeO content of melts increases with F, but at high pressures the FeO content of melts decreases with F. The coefficients in Table 2 are optimized after multiple-regression analysis in order to place greater emphasis on the higher-pressure results of *Jaques and Green* [1980] and *Falloon et al.* [1988]. The behavior of these oxides in calculated batch melts from HPY and TQL are shown in Figures 8*a* and 8*b*.

However, neither HPY nor TQL is a good candidate for the mantle source of most MORB magmas. *Falloon and Green* [1987] showed that, in fact, these two peridotites probably represent extremes of a spectrum of peridotites likely to be

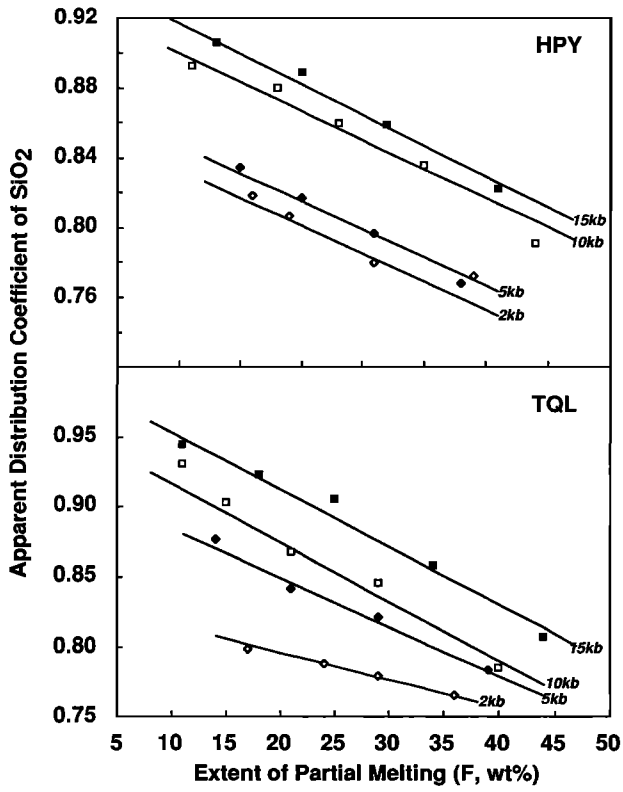

Fig. 5. Plots of D_{SiO_2} versus F(weight percent) for HPY and TQL. The 2-kbar and 10-kbar data for HPY show slight deviations at high F (>40%). For this reason, we place less emphasis on F > 40% and P < 5 kbar. Plots of this type were made for all elements and used to empirically determine the form of (6) and its coefficients.

found in the suboceanic mantle (Table 3). HPY is probably too rich in Na_2O, K_2O, and TiO_2 and too poor in CaO to be a good candidate for MORB mantle. Likewise, TQL is probably too poor in Na_2O and K_2O. From the mantle array analysis of *Falloon and Green* [1987], MORB pyrolite with Fo_{90} (MPY-90) appears to be the best candidate for the MORB source.

Unfortunately, the experiments on MPY-90 by *Falloon and Green* [1987, 1988] are sandwich experiments, so F was not determined from each run. Furthermore, the number of runs and the P-T coverage of MPY-90's behavior are insufficient to carry out the sort of analysis we performed for HPY and TQL. Instead, we used the equation (6) coefficients (*e* - *i*) for TQL as a starting point and by trial and error varied them to fit the available data for MPY-90. The coefficients listed in Table 4 are the results of this attempt. Because TQL and MPY-90 are very similar in bulk composition, we use the equation (5) coefficients of TQL (Table 1) for MPY-90. While the fit of the Table 4 coefficients to MPY-90 behavior cannot be verified at the same level of confidence as for HPY and TQL, we are confident that these values are reasonably good. Figure 8*c* shows the calculated melt compositions for MPY-90 as a function of P and F.

Isobaric Batch Melting Model

Figures 8*a*, 8*b*, and 8*c* show the calculated isobaric batch melts from HPY, TQL, and MPY-90. These are calculated using (11) of Shaw [1970] with F and D_i values from (5) and (6) and the data of Tables 1, 2, and 4. Each oxide is calculated independently, and the melt compositions (not shown in tabulated form) sum to 100% ± 2%. Our extrapolation of the results of *Jaques and Green* [1980] from 15 kbar to 20 kbar is in excellent agreement with the results of *Falloon et al.* [1988] and *Falloon and Green* [1988] at 20 kbars and higher.

In addition to the conclusions reached by *Jaques and Green* [1980], it is worth making some additional points about the characteristics of isobaric batch melts. First, it is clear that melt concentrations of SiO_2, Al_2O_3, FeO, and MgO are affected by pressure. However, the effect can be complex, and F can exert an important control, as for FeO. CaO melt concentration reaches a maximum before clinopyroxene is consumed. Because melt composition can be strongly affected by both P and F, caution must be taken in inferring the P and F of formation of natural MORB glasses on the basis of a single oxide. In addition, of course, the bulk composition of the peridotite source can exert a significant effect, as shown by *Langmuir and Hanson* [1980*a*]. A comparison among Figures 8*a*, 8*b*, and 8*c* illustrates the potential effect from source heterogeneity.

Decompression-Induced Column Melting Model

As discussed previously, MORB melts are probably not produced by isobaric batch melting. Instead, melting is probably polybaric and occurs in response to adiabatic ascent of solid mantle material. At the same time, melt escapes the system and can accumulate by segregation processes. It is this process of column melting due to decompression of upwelling mantle that we wish to approximate in our model. We stress that available data allow only an approximation to this process and several uncertainties are present.

We attempt to model the melts produced by a parcel of mantle rising adiabatically and melting continuously along the idealized adiabatic paths shown in Figure 9. The very low melt retention in the mantle and the relatively rapid melt extraction process [*McKenzie*, 1984, 1985*b*] imply that melting and melt extraction occur continuously in the mantle. Thus, melting can be considered as a series of infinitesimally small incremental batches in the course of continuous melting accompanied by instantaneous melt extraction. These incremental batches may aggregate or accumulate to form MORB melts. The composition of each oxide in the accumulated melt can ideally be evaluated by

$$C_i^l = \frac{1}{F}\int_0^F \frac{C_i^R}{F + D_i\,(1 - F)}\,dF \qquad (7)$$

where C_i^l is the concentration of i in the accumulated melt when the total amount of melting reaches F along an adiabatic ascent path, C_i^R is the concentration of oxide i in the solid residue at F, and D_i is the apparent bulk distribution coefficient of i. The integrand, the concentration of i of the incremental batch, implies that at any instance in the course of the continuous melting, only a finite amount of melt (dF) is in equilibrium with solid residue. Since $D_i = f(F,P)$ and $C_i^R = f(F,D_i)$, (7) cannot be solved analytically. We thus solve (7) numerically by finite difference. For simplicity and because of lack of data for small degree melts, the first melt we produce is a 5% isobaric batch melt which is followed by incremental steps of dF = 0.01 (1%). In each step, C_i^R, the residue, is calculated by mass balance, and it serves as the source for the next increment of melting. The D_i values are recalculated in response to the changes in P and F at each step. We calculate

Table 2. Empirical Coefficients Determined For Apparent Bulk Distribution Coefficients

Oxide	Hawaiian Pyrolite						Tinaquillo Lherzolite					
	e	*f*	*g*	*h*	*i*	R^{2*}	*e*	*f*	*g*	*h*	*i*	R^{2*}
SiO_2	0.8788 (±0.0430)	- 0.0031 (±0.0020)	0	0.0060 (±0.0020)	0	0.977	0.8840 (±0.0610)	- 0.0030 (±0.0020)	0	0.0060 (0.002)	0	0.973
TiO_2	0.0910 (±0.0020)	- 0.0020 (±0.0010)	0	0	0	0.974			0	0	0	0.974†
Al_2O_3	0.0812 (±0.0061)	- 0.0031 (±0.0001)	0.1253 (±0.0410)	0.0050 (±0.0010)	0	0.955	0.0682 (±0.0091)	- 0.0030 (±0.0080)	0.0520 (±0.0110)	0.0050 (±0.0010)	0	0.931
FeO	1.6091 (±0.2310)	-0.0181 (±0.0081)	0	0.01210 (±0.0060)	-0.8661 (±0.1380)	0.947	1.5804 (±0.2310)	-0.0192 (±0.003)	0	0.0061 (±0.003)	-0.6190 (±0.1010)	0.932
MgO	6.6463 (±0.5111)	- 0.0842 (±0.0070)	0	- 0.0760 (±0.009)	0	0.948	4.6234 (±0.4203)	- 0.0500 (±0.0060)	0	-0.0542 (±0.0040)	0	0.926
CaO	- 0.4751 (±0.0310)	0.0059 (±0.0011)	10.1521 (±1.4312)	0.0005 (±0.0002)	0	0.956	-0.1015 (±0.0210)	0.0022 (±0.0007)	3.4592 (±0.3321)	0.0005 (±0.0003)	0	0.929
Na_2O	0.0991 (±0.0080)	- 0.0042 (±0.0012)	0	0	0	0.993	0.0509 (±0.0090)	- 0.0038 (±0.0008)	0	0	0	0.993
K_2O	0.0099 (±0.001)	- 0.0002 (±2.00e-5)	0	0	0	0.994			0	0	0	0.994†
CaO‡	0.3110	- 0.0081	0.3071	0.0005	0		0.2610	- 0.0091	0.4407	0.0005	0	
FeO‡	0.9121	0	2.2670	-0.0210	-0.1213		0.8361	0	2.2870	-0.0141	-0.1922	

$D_i = e + fF + g/F + h\,P + i\,P/F$ is the general form to describe partitioning behavior for all the oxides. No units are necessary for the nondimensional D_i as each of the coefficients will take the reciprocal form of the corresponding variables and will be cancelled out.

*R^2 and uncertainties listed are from regression of the raw data.

† The concentration of TiO_2 and K_2O for Tinaquillo Lherzolite and experimental melts are too low to determine, so the coefficients for Hawaiian Pyrolite are used.

‡Recommended values for CaO and FeO to extrapolate the experimental data down to ~5% melting without affecting the melting ranges where data are available.

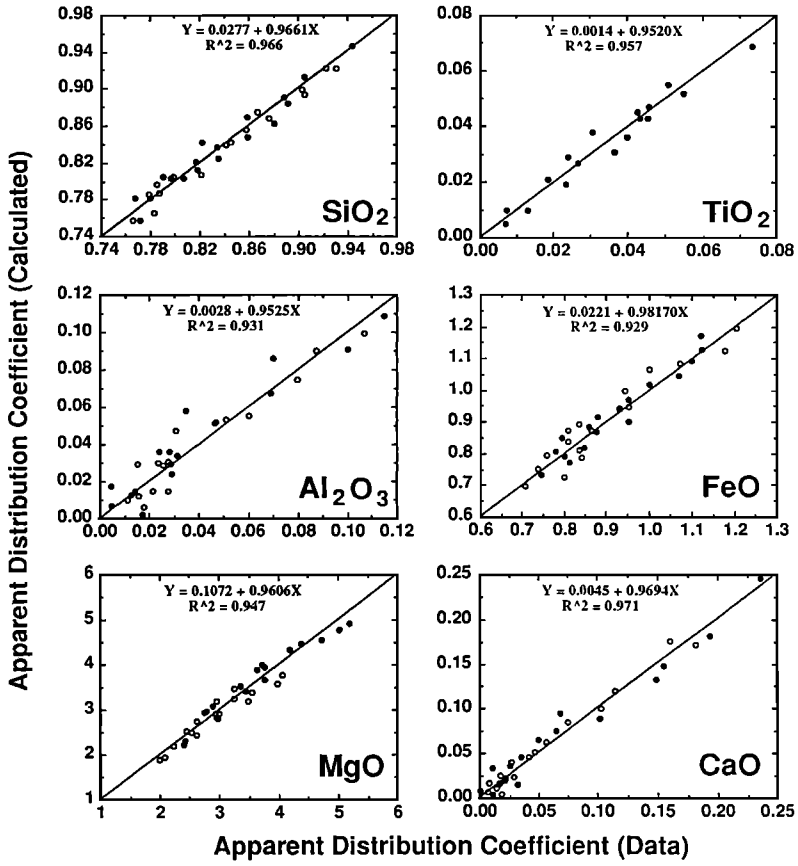

Fig. 6. A comparison between D_i calculated using (6) and D_i directly derived from experiments (equation (3)) for both HPY (solid circles) and TQL (open circles). The *Jaques and Green* [1980] data and *Falloon et al.* [1988] data are corrected using the results of Figure 1. For TiO_2, only HPY data are plotted, since TiO_2 values for TQL are too uncertain to be of value. D_{Na_2O} and D_{K_2O} are omitted because no mass balance could be obtained using the experimental results. Even so, (6) is able to reproduce available abundances in both HPY and TQL (see Figure 7). The equations are for the regression lines.

the accumulated melt compositions at each increment along the adiabat corresponding to eight initial pressures (P_o = 20, 18, 16, 14, 12, 10, 8, and 6 kbar) at which upwelling mantle may cross the solidus as shown in Figure 9. Since we have no constraints at this stage on the depth where melting stops (P_f), we continue melting to a depth of ~2–3 kbar.

One major assumption in this model is the use of bulk D_i values derived from isobaric batch melting. This may not be directly applicable to column melting because of the progressive depletion that the source undergoes and because the compositional effects on instantaneous D_i values may differ from those in isobaric batch melting. To partly ameliorate this effect, we obtained a new set of empirical coefficients for (6), given in Table 5. They were derived from Table 4 by a very laborious iterative process of optimization of the "analytical" sums of oxides for each incremental melt along each of the eight adiabatic melting paths (a total of 155 incremental melts were considered) without affecting the compositions of the initial 5% isobaric batch melts.

Another potential problem is that we assume that each melt parcel follows the adiabatic melting paths shown in Figure 9. The slope of this adiabat and its temperature are not precisely known, but can have an important effect on the amount of melt produced. Also, because of the compositional changes that occur in the solid during melting, it is unlikely that the model adiabat (which should be curved) will be followed strictly. Whether polybaric column melting takes place in equilibrium with a small amount of interstitial liquid (continuous melting as defined by *Langmuir et al.* [1977]) or not (i.e., fractional melting), the continual depletion of the solid will affect its melting path. It is possible, for example, that melting to produce MORB occurs very close to the solidus throughout the melting interval. This effect is probably very important in determining the pressure at which melting ceases (discussed later) and underscores the importance of obtaining more experimental data, especially at small degrees of melting for a variety of depleted peridotite compositions. Note that our physical model for column melting is highly generalized and does not explicitly consider the geometry of the melting region, melt migration path, and a variety of other issues. This is deliberate, as geometric parameters and melt distribution are poorly known, however, more specific physical models are available (e.g. Plank and Langmuir, 1991).

With these uncertainties in mind, and with (5)–(7), and the coefficients from Tables 1 and 5, we calculate the pooled or accumulated column melts. These are shown in Table 6 and presented graphically in Figure 10. These simulated melts are derived from MPY-90, and, as before, each oxide component is calculated independently.

Accumulated polybaric column melts are different in several important ways from isobaric batch melts as can be seen by comparing Figures 8 and 10. The pressure effects on SiO_2, Al_2O_3, FeO, and MgO are larger for the accumulated melts than for batch melts. SiO_2 also increases faster with increasing F than in the batch melts. No picritic melts are produced in the range of P and F that we have investigated. FeO in the accumulated melts does not increase with F at any initial pressure (in contrast to the batch melts, in which FeO increases

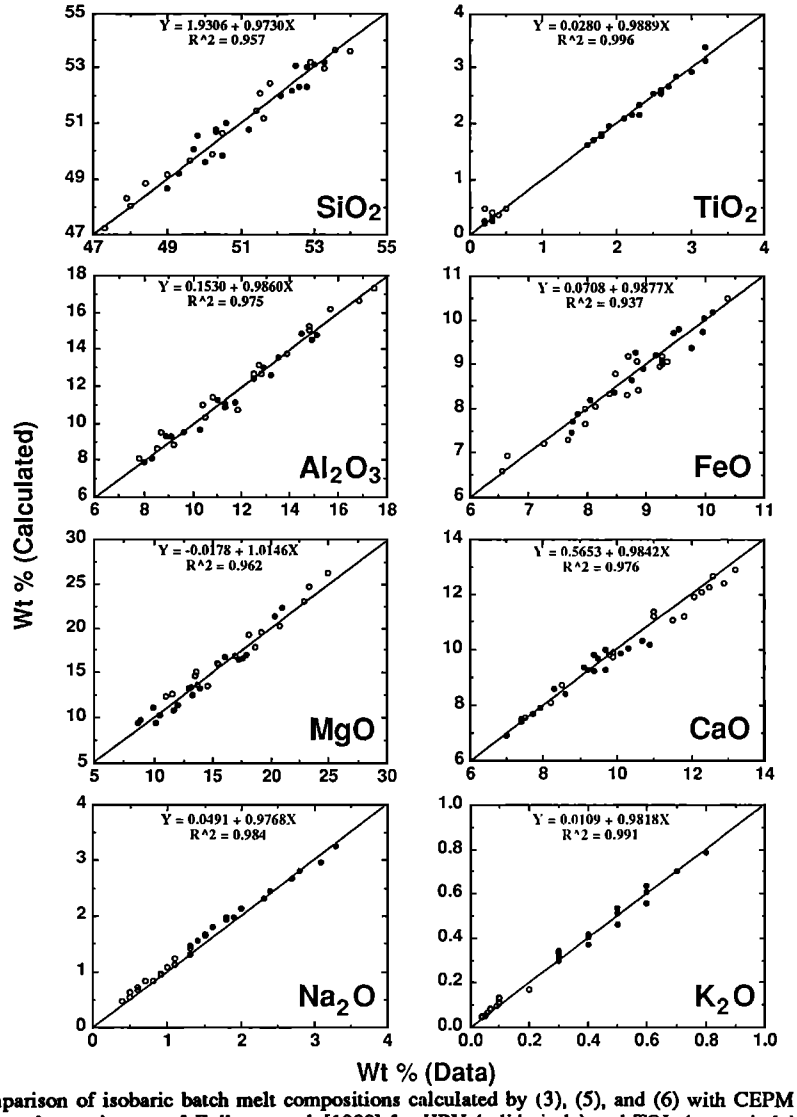

Fig. 7. A comparison of isobaric batch melt compositions calculated by (3), (5), and (6) with CEPM of *Jaques and Green* [1980] and reversal experiments of *Falloon et al.* [1988] for HPY (solid circle) and TQL (open circle). Note that with a few exceptions typical departures from the 1:1 agreement are of the order of analytical uncertainty.

with F at lower pressures). CaO does not have a maximum for accumulated melts, as aggregation tends to buffer drastic change in melt composition. As expected, TiO_2, Na_2O, and K_2O in accumulated melts are higher at lower F and decrease faster than in batch melts. This is also true for Al_2O_3, but the decrease is balanced by increasing Al_2O_3 in the melts as pressure decreases along the melting paths.

The normative compositions of accumulated melts also differ greatly from the batch melts. None are quartz normative even at the lowest initial melting pressures (P_o). Very few are highly depleted in Hy or have normative Ne. Overall most accumulated melts produced at F = 10–20% and P_o = 6–20 kbar are Ol-Hy normative.

Application

In order to apply our calculated polybaric column melts to natural MORB melts for interpretation, we follow *Klein and Langmuir* [1987] in choosing a reference level of MgO = 8.0 wt %. We fractionated our primary melts to 8.0 wt % MgO using the low-pressure liquid lines of descent algorithm of *Weaver and Langmuir* [1990]. For natural MORBs with MgO < 8.0 wt %, we correct for fractionation as described by *Klein and Langmuir* [1987] along individual liquid lines of descent appropriate to each locality. A reference level of MgO = 8.0 wt % is reasonable, since the MgO range of our computed primary column melts is small (9–12 wt %). In most cases, fractionation involves only a small amount of olivine and plagioclase subtraction. We also assume that the mantle source of MORB is homogeneous with respect to major elements.

Implicitly, we also assume high-pressure fractionation in the mantle is a minor process for MORB genesis. Many lines of evidence suggest that MORB melts rise quickly and do not reequilibrate extensively during ascent. Several arguments can also be made for the importance of high pressure fractionation at a variety of pressures [e.g., *Elthon* et al. 1982; Kinzler and Grove, 1991], however in this study we do not find it necessary to invoke this process.

Figure 11 shows the accumulated melts (Table 6, Figure 10) fractionated to an MgO value of 8.0 wt %. We use the subscript 8 to denote the value of other oxides at 8.0 wt % MgO. Many of the patterns seen in Figure 10 are still evident for the fractionated accumulated melts, but there are also some important differences. For example, the pressure dependence of Al_2O_3 and CaO for the fractionated melts is opposite to that for unfractionated melts. This is to be expected, as in this model, higher-pressure primary melts are more MgO-rich and thus fractionate more olivine to achieve higher enrichments of CaO and Al_2O_3 than lower-pressure melts that crystallize a higher

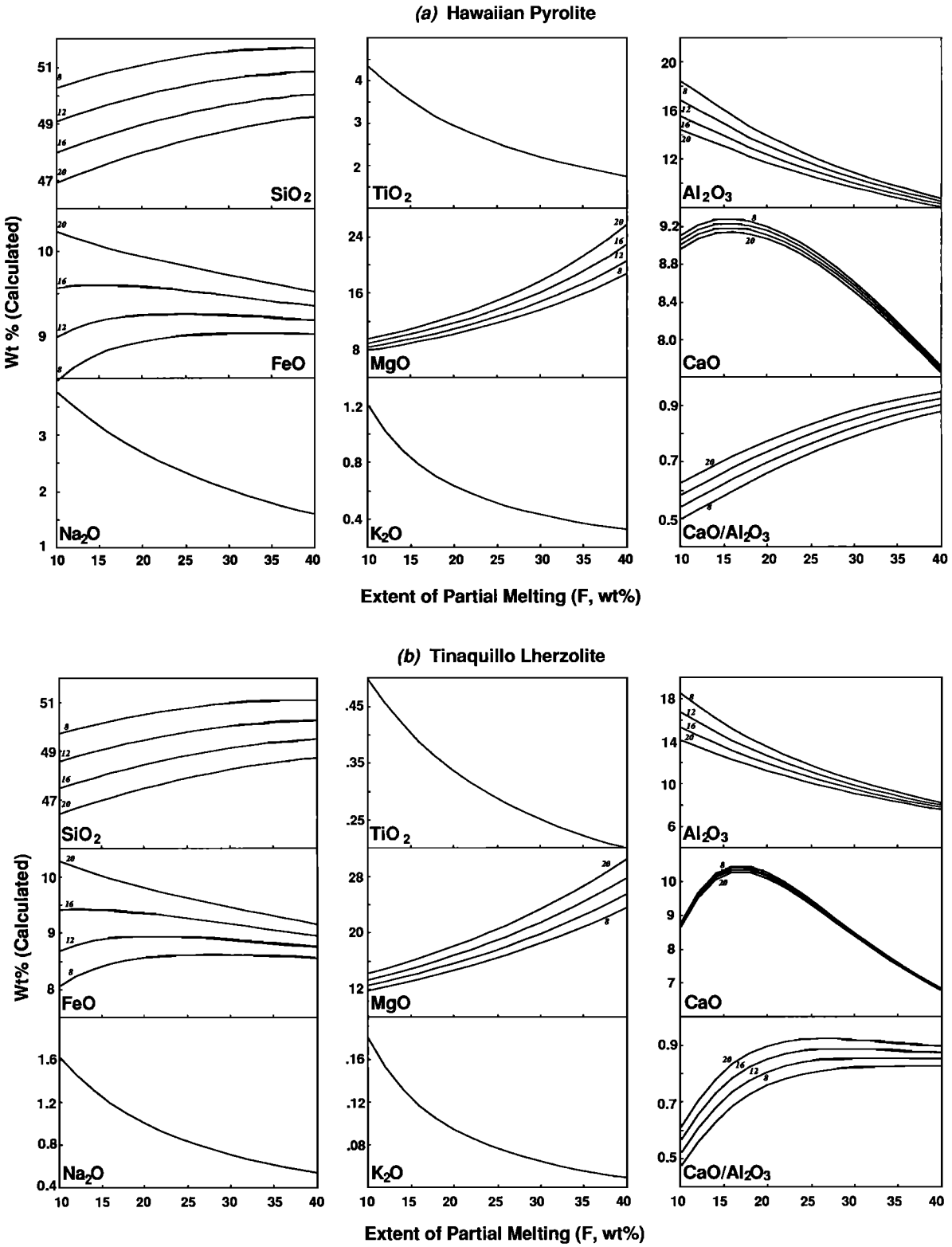

Fig. 8. Calculated isobaric melt compositions for (*a*) HPY, (*b*) TQL, and (*c*) MPY-90. The results are plotted to show the behavior of each oxide component in the melts with pressure (labeled with small numbers in kilobars) and extent of partial melting (F). See text for discussion.

proportion of plagioclase at low pressure. For fractionated melts, the decrease of FeO with increasing F is more pronounced, and the overall concentrations of SiO_2 are higher as expected from olivine and plagioclase fractionation.

The next step toward applying our model results to natural MORBs is to find a good chemical discriminant for initial melting pressure (P_o). Figure 11 shows that both $Si_{(8)}$ and $Fe_{(8)}$ are sensitive to pressure, but in an opposite sense. Thus, to optimize the sensitivity, we use the ratio $Si_{(8)}/Fe_{(8)}$ as a pressure indicator. Figure 12*a* shows that this ratio varies

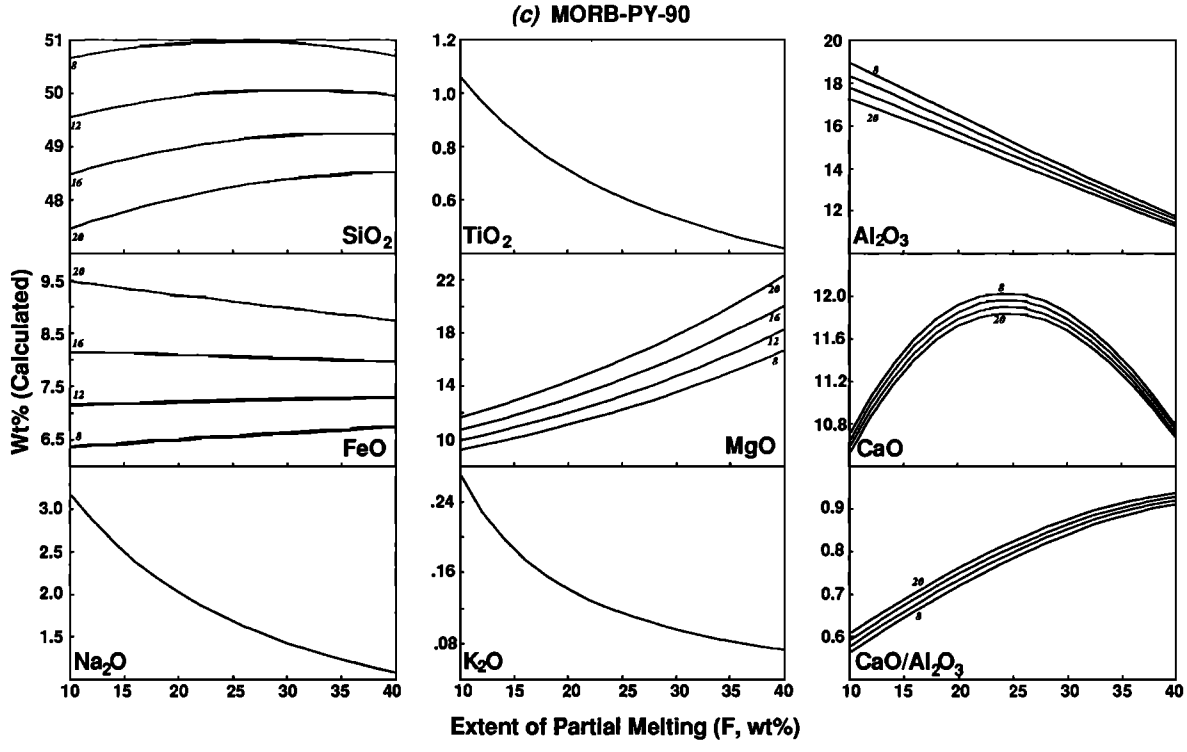

Fig. 8. (continued)

Table 3. Compositions Of Source Materials Investigated

Oxide	HPY	TQL	MPY-90	
SiO_2	45.20	44.95	44.74	(44.50–45.60)
TiO_2	0.71	0.08	0.17	(0.10–0.35)
Al_2O_3	3.54	3.22	4.37	(3.85–4.44)
FeO	8.47	7.66	7.55	(7.40–8.40)
MgO	37.50	40.03	38.57	(37.50–39.5)
CaO	3.08	2.99	3.38	(3.05–4.00)
Na_2O	0.57	0.18	0.40	(0.35–0.42)
K_2O	0.13	0.02	0.03*	(0.02–0.08)
Total	99.20	99.13	99.22	

Data for HPY and TQL are from *Jaques and Green* [1980] and for MPY-90 are from *Falloon and Green* [1987]. In the parenthesis after MPY-90 are compositional ranges for which the coefficients in Tables 4 and 5 may apply.
*Assumed K_2O content for MPY-90 in our calculations.

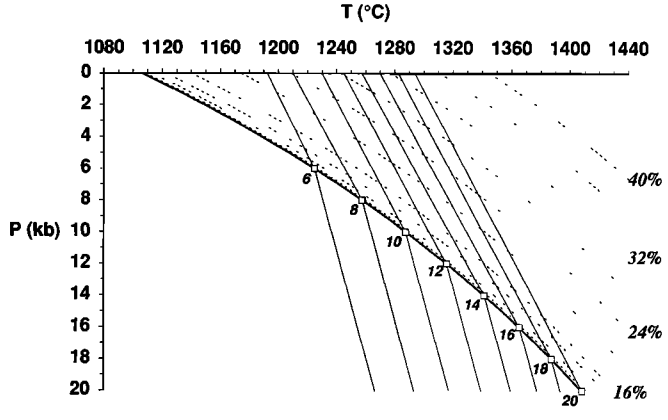

Fig. 9. Adiabatic melting paths (light solid lines) in P-T space. The solidus (heavy solid line) and melting (F) isopleths are from Figure 4*b*. The adiabat gradients (3° Kar^{-1} for solid and 6° Kar^{-1} after initial melting) are from *McKenzie* [1984]. The initial melting (P_o) for each path is indicated.

rather smoothly with F and P. This allows us to quantify, for each melting path, the relationship between P_o and F. We find the expression

$$P_o(kb) = 25.98 + 0.967\,F + 45.277\,\frac{1}{F} - 5.186\,\frac{Si_{(8)}}{Fe_{(8)}} \quad (8)$$

fits the data very well. To use (8), we need to determine F independently. For this we use $Na_{(8)}$ and $Ca_{(8)}/Al_{(8)}$, which, as shown in Figures 11 and 12*b*, are insensitive to pressure, but highly dependent on F [see also *Natland* 1989]. $Ti_{(8)}$ and $K_{(8)}$ also would be good choices, but their abundances in MPY-90 are not as well constrained as Na_2O, Al_2O_3, and CaO. From the observed variation of $Na_{(8)}$ and $Ca_{(8)}/Al_{(8)}$) in fractionated accumulated column melts, we derive the expression:

Table 4. Estimated Coefficients for MPY-90

Oxide	*e*	*f*	*g*	*h*	*i*
SiO_2	0.8480	- 0.0022	0	0.0055	0
TiO_2	0.0910	- 0.0020	0	0	0
Al_2O_3	0.1960	- 0.0065	-0.0250	0.0021	0
FeO	1.4720	0	0.2730	- 0.0350	-0.0130
MgO	5.6230	- 0.0451	0	- 0.0810	0
CaO	0.3270	- 0.0120	0.3071	0.0005	0
Na_2O	0.0509	- 0.0038	0	0	0
K_2O*	0.0099	- 0.0002	0	0	0

These coefficients are obtained by trial and error to fit the experimental data for MPY-90 [*Falloon and Green*, 1987, 1988]. The uncertainties for the coefficients are probably of the same order as the regression errors for TQL (Table 2).

*Treated the same as for Tinaquillo Lherzolite.

Table 5. Recommended Coefficients for MPY-40

Oxide	*e*	*f*	*g*	*h*	*i*
SiO_2	0.8580	- 0.0040	0	0.0050	0
TiO_2	0.0980	- 0.0050	0	0	0
Al_2O_3	0.1890	- 0.0051	-0.0250	0.0021	0
FeO	1.4420	0	0.2730	- 0.0350	-0.0130
MgO	5.2860	- 0.0640	0	- 0.0630	0
CaO	0.3180	- 0.0122	0.2720	0.0005	0
Na_2O	0.1110	- 0.0070	0	0	0
K_2O*	0.0690	- 0.0020	0	0	0

*The same as for Table 4. See text for discussion of how these coefficients are obtained.

Table 6. Oxide Compositions and CIPW Norms of Accumulated melts

F*	T†	P_f‡	SiO_2	TiO_2	Al_2O_3	FeO	MgO	CaO	Na_2O	K_2O	Sum	$\frac{CaO}{Al_2O_3}$	Mg#	Or	Ab	An	Ne	Di	Hy	Ol	Mt	Il
Initial Melting At 20 kbar																						
6	1406	19.41	47.47	1.42	18.17	9.98	10.67	9.16	3.27	0.35	100.50	0.50	67.93	2.04	22.84	33.90	2.60	9.33	0.00	25.58	1.61	2.70
8	1402	18.70	47.60	1.37	17.95	9.96	10.88	9.43	3.19	0.30	100.68	0.53	68.40	1.74	22.55	33.79	2.42	10.52	0.00	25.57	1.60	2.59
10	1397	17.85	47.74	1.29	17.68	9.93	11.13	9.72	3.08	0.26	100.83	0.55	68.95	1.52	22.23	33.63	2.09	11.81	0.00	25.60	1.60	2.46
12	1391	16.87	47.90	1.21	17.36	9.88	11.40	10.01	2.94	0.23	100.93	0.58	69.56	1.34	21.96	33.52	1.57	13.06	0.00	25.68	1.59	2.30
14	1384	15.76	48.08	1.13	17.04	9.80	11.67	10.31	2.75	0.20	100.97	0.60	70.23	1.20	21.86	33.54	0.77	14.22	0.00	25.77	1.58	2.14
16	1376	14.51	48.34	1.03	16.74	9.61	11.88	10.62	2.48	0.18	100.88	0.63	71.00	1.07	20.95	34.03	0.00	15.05	2.24	24.13	1.55	1.96
18	1368	13.12	48.67	0.94	16.46	9.36	12.04	10.95	2.20	0.16	100.79	0.67	71.81	0.97	18.62	34.54	0.00	15.95	7.10	20.42	1.51	1.79
20	1359	11.60	49.02	0.85	16.14	9.12	12.20	11.28	1.98	0.15	100.74	0.70	72.61	0.88	16.76	34.71	0.00	17.14	10.90	17.37	1.47	1.61
22	1349	9.95	49.37	0.77	15.79	8.88	12.36	11.63	1.80	0.14	100.74	0.74	73.38	0.80	15.23	34.61	0.00	18.59	13.93	14.78	1.43	1.47
24	1338	8.16	49.74	0.71	15.40	8.66	12.51	11.98	1.65	0.12	100.78	0.78	74.12	0.74	13.96	34.25	0.00	20.27	16.39	12.53	1.39	1.34
26	1327	6.23	50.11	0.65	14.97	8.44	12.67	12.34	1.52	0.12	100.83	0.82	74.83	0.68	12.89	33.67	0.00	22.14	18.41	10.53	1.36	1.24
28	1314	4.17	50.48	0.61	14.49	8.24	12.83	12.07	1.41	0.11	100.24	0.83	75.51	0.63	11.97	32.88	0.00	21.67	23.72	6.98	1.33	1.15
Initial Melting At 18 kbar																						
6	1385	17.37	47.96	1.42	18.46	9.11	10.33	9.20	3.27	0.35	100.11	0.50	69.19	2.04	24.78	34.69	1.55	8.86	0.00	24.10	1.47	2.70
8	1381	16.72	48.08	1.37	18.23	9.10	10.53	9.48	3.19	0.30	100.28	0.52	69.61	1.74	24.49	34.55	1.37	10.08	0.00	24.08	1.47	2.59
10	1376	15.94	48.22	1.29	17.94	9.09	10.76	9.78	3.08	0.26	100.43	0.54	70.10	1.52	24.17	34.37	1.04	11.41	0.00	24.11	1.46	2.46
12	1371	15.03	48.38	1.21	17.62	9.06	11.01	10.07	2.94	0.23	100.52	0.57	70.65	1.34	23.90	34.22	0.52	12.71	0.00	24.17	1.46	2.30
14	1365	13.98	48.55	1.13	17.28	9.01	11.27	10.37	2.75	0.20	100.56	0.60	71.25	1.20	23.29	34.19	0.00	13.91	0.84	23.64	1.45	2.14
16	1358	12.81	48.81	1.03	16.96	8.86	11.48	10.68	2.48	0.18	100.49	0.63	71.95	1.07	20.95	34.64	0.00	14.79	5.39	20.36	1.43	1.96
18	1350	11.51	49.13	0.94	16.65	8.67	11.64	11.01	2.20	0.16	100.41	0.66	72.69	0.97	18.62	35.08	0.00	15.74	10.12	16.80	1.40	1.79
20	1341	10.07	49.47	0.85	16.31	8.47	11.81	11.35	1.98	0.15	100.39	0.70	73.41	0.88	16.76	35.19	0.00	16.99	13.81	13.88	1.37	1.61
22	1332	8.50	49.81	0.77	15.94	8.28	11.97	11.69	1.80	0.14	100.41	0.73	74.11	0.80	15.23	35.01	0.00	18.49	16.74	11.42	1.33	1.47
24	1322	6.81	50.16	0.71	15.53	8.10	12.13	12.04	1.65	0.12	100.45	0.78	74.79	0.74	13.96	34.59	0.00	20.21	19.11	9.28	1.31	1.34
26	1311	4.98	50.52	0.65	15.07	7.93	12.30	12.39	1.52	0.12	100.50	0.82	75.45	0.68	12.89	33.94	0.00	22.12	21.05	7.38	1.28	1.24
28	1299	3.02	50.87	0.61	14.57	7.76	12.46	12.11	1.41	0.11	99.91	0.83	76.08	0.63	11.97	33.08	0.00	21.69	26.30	3.92	1.25	1.15
Initial Melting At 16 kbar																						
6	1362	15.36	48.45	1.42	18.76	8.38	10.01	9.25	3.27	0.35	99.90	0.49	70.29	2.04	26.59	35.51	0.57	8.38	0.00	22.84	1.35	2.70
8	1359	14.78	48.58	1.37	18.52	8.39	10.19	9.53	3.19	0.30	100.07	0.51	70.66	1.74	26.30	35.34	0.39	9.63	0.00	22.80	1.35	2.59
10	1355	14.07	48.71	1.29	18.22	8.38	10.42	9.83	3.08	0.26	100.20	0.54	71.11	1.52	25.98	35.12	0.05	11.00	0.00	22.81	1.35	2.46
12	1350	13.23	48.87	1.21	17.88	8.37	10.66	10.13	2.94	0.23	100.28	0.57	71.60	1.34	24.86	34.93	0.00	12.34	1.42	21.83	1.35	2.30
14	1344	12.26	49.04	1.13	17.52	8.34	10.90	10.43	2.75	0.20	100.31	0.60	72.15	1.20	23.29	34.86	0.00	13.59	3.82	20.17	1.34	2.14
16	1337	11.16	49.29	1.03	17.19	8.23	11.11	10.74	2.48	0.18	100.24	0.63	72.78	1.07	20.95	35.25	0.00	14.53	8.30	16.95	1.33	1.96
18	1330	9.93	49.60	0.94	16.85	8.08	11.28	11.07	2.20	0.16	100.18	0.66	73.45	0.97	18.62	35.62	0.00	15.53	12.93	13.50	1.30	1.79
20	1322	8.57	49.92	0.85	16.49	7.92	11.44	11.41	1.98	0.15	100.16	0.69	74.11	0.88	16.76	35.66	0.00	16.83	16.53	10.69	1.28	1.61
22	1313	7.08	50.25	0.77	16.09	7.77	11.61	11.75	1.80	0.14	100.18	0.73	74.75	0.80	15.23	35.42	0.00	18.38	19.38	8.33	1.25	1.47
24	1303	5.46	50.59	0.71	15.65	7.62	11.78	12.10	1.65	0.12	100.22	0.77	75.38	0.74	13.96	34.93	0.00	20.15	21.66	6.28	1.23	1.34
26	1292	3.71	50.93	0.65	15.17	7.48	11.95	12.45	1.52	0.12	100.26	0.82	75.99	0.68	12.89	34.21	0.00	22.11	23.55	4.46	1.21	1.24
Initial Melting At 14 kbar																						
6	1338	13.39	48.96	1.42	19.07	7.76	9.70	9.30	3.27	0.35	99.83	0.49	71.25	2.04	27.65	36.35	0.00	7.89	1.07	20.96	1.25	2.70
8	1335	12.88	49.08	1.37	18.82	7.77	9.88	9.58	3.19	0.30	100.00	0.51	71.59	1.74	27.01	36.16	0.00	9.17	1.64	20.51	1.25	2.59
10	1331	12.24	49.22	1.29	18.50	7.78	10.09	9.89	3.08	0.26	100.11	0.53	71.99	1.52	26.08	35.90	0.00	10.58	2.66	19.76	1.25	2.46
12	1327	11.48	49.37	1.21	18.15	7.78	10.32	10.19	2.94	0.23	100.18	0.56	72.44	1.34	24.86	35.66	0.00	11.97	4.24	18.64	1.25	2.30
14	1321	10.58	49.54	1.13	17.77	7.76	10.56	10.49	2.75	0.20	100.19	0.59	72.94	1.20	23.29	35.54	0.00	13.27	6.62	16.97	1.25	2.14
16	1315	9.54	49.77	1.03	17.41	7.68	10.76	10.80	2.48	0.18	100.12	0.62	73.51	1.07	20.95	35.86	0.00	14.26	11.04	13.83	1.24	1.96
18	1308	8.38	50.07	0.94	17.05	7.56	10.93	11.13	2.20	0.16	100.06	0.65	74.12	0.97	18.62	36.17	0.00	15.32	15.59	10.47	1.22	1.79
20	1300	7.09	50.38	0.85	16.67	7.44	11.10	11.47	1.98	0.15	100.03	0.69	74.72	0.88	16.76	36.14	0.00	16.68	19.11	7.74	1.20	1.61
22	1292	5.67	50.69	0.77	16.24	7.32	11.27	11.81	1.80	0.14	100.05	0.73	75.32	0.80	15.23	35.83	0.00	18.28	21.88	5.45	1.18	1.47
24	1283	4.11	51.01	0.71	15.78	7.20	11.45	12.16	1.65	0.12	100.08	0.77	75.90	0.74	13.96	35.27	0.00	20.10	24.10	3.48	1.16	1.34

Table 6. (Continued)

F*	T†	P_f‡	SiO_2	TiO_2	Al_2O_3	FeO	MgO	CaO	Na_2O	K_2O	Sum	$\frac{CaO}{Al_2O_3}$	$Mg^{\#}$	Or	Ab	An	Ne	Di	Hy	Ol	Mt	Il
											Initial Melting At 12 kbar											
6	1312	11.45	49.48	1.42	19.39	7.22	9.42	9.35	3.27	0.35	99.90	0.48	72.10	2.04	27.65	37.22	0.00	7.37	3.74	18.08	1.16	2.70
8	1310	11.03	49.60	1.37	19.13	7.24	9.59	9.64	3.19	0.30	100.05	0.50	72.40	1.74	27.01	37.00	0.00	8.69	4.31	17.61	1.17	2.59
10	1306	10.46	49.73	1.29	18.80	7.26	9.79	9.94	3.08	0.26	100.15	0.53	72.77	1.52	26.08	36.70	0.00	10.14	5.33	16.84	1.17	2.46
12	1302	9.77	49.88	1.21	18.42	7.26	10.01	10.25	2.94	0.23	100.20	0.56	73.19	1.34	24.86	36.41	0.00	11.58	6.92	15.69	1.17	2.30
14	1297	8.94	50.04	1.13	18.03	7.26	10.23	10.55	2.75	0.20	100.19	0.59	73.64	1.20	23.29	36.24	0.00	12.93	9.30	14.01	1.17	2.14
16	1292	7.97	50.28	1.03	17.65	7.20	10.43	10.87	2.48	0.18	100.11	0.62	74.17	1.07	20.95	36.51	0.00	13.98	13.68	10.88	1.16	1.96
18	1285	6.87	50.55	0.94	17.26	7.11	10.60	11.20	2.20	0.16	100.03	0.65	74.72	0.97	18.62	36.74	0.00	15.11	18.15	7.60	1.15	1.79
20	1278	5.64	50.85	0.85	16.85	7.01	10.78	11.53	1.98	0.15	100.00	0.68	75.28	0.88	16.76	36.64	0.00	16.52	21.60	4.94	1.13	1.61
22	1269	4.27	51.15	0.77	16.39	6.92	10.95	11.88	1.80	0.14	100.00	0.72	75.83	0.80	15.23	36.25	0.00	18.18	24.31	2.71	1.11	1.47
											Initial Melting At 10 kbar											
6	1285	9.55	50.01	1.42	19.72	6.75	9.15	9.40	3.27	0.35	100.07	0.48	72.86	2.04	27.65	38.12	0.00	6.84	6.29	15.41	1.09	2.70
8	1283	9.21	50.12	1.37	19.45	6.78	9.31	9.69	3.19	0.30	100.21	0.50	73.13	1.74	27.01	37.87	0.00	8.19	6.86	14.92	1.09	2.59
10	1280	8.73	50.25	1.29	19.10	6.80	9.50	10.00	3.08	0.26	100.29	0.52	73.47	1.52	26.08	37.52	0.00	9.69	7.88	14.12	1.10	2.46
12	1276	8.11	50.40	1.21	18.71	6.81	9.71	10.30	2.94	0.23	100.31	0.55	73.85	1.34	24.86	37.19	0.00	11.18	9.47	12.95	1.10	2.30
14	1272	7.34	50.56	1.13	18.29	6.82	9.93	10.61	2.75	0.20	100.29	0.58	74.27	1.20	23.29	36.95	0.00	12.59	11.84	11.25	1.10	2.14
16	1266	6.44	50.77	1.03	17.88	6.78	10.13	10.93	2.48	0.18	100.18	0.61	74.75	1.07	20.95	37.14	0.00	13.70	16.16	8.17	1.09	1.96
18	1260	5.40	51.04	0.94	17.47	6.71	10.30	11.26	2.20	0.16	100.09	0.64	75.26	0.97	18.62	37.31	0.00	14.89	20.58	4.94	1.08	1.79
20	1253	4.22	51.32	0.85	17.03	6.64	10.48	11.60	1.98	0.15	100.04	0.68	75.77	0.88	16.76	37.13	0.00	16.36	23.97	2.33	1.07	1.61
											Initial Melting At 8 kbar											
6	1256	7.68	50.55	1.42	20.06	6.34	8.90	9.45	3.27	0.35	100.34	0.47	73.53	2.04	27.65	39.05	0.00	6.29	8.74	12.91	1.02	2.70
8	1254	7.43	50.66	1.37	19.78	6.37	9.05	9.74	3.19	0.30	100.46	0.49	73.79	1.74	27.01	38.77	0.00	7.68	9.31	12.40	1.03	2.59
10	1252	7.03	50.79	1.29	19.41	6.40	9.23	10.05	3.08	0.26	100.52	0.52	74.10	1.52	26.08	38.38	0.00	9.22	10.34	11.57	1.03	2.46
12	1249	6.49	50.93	1.21	19.00	6.42	9.44	10.36	2.94	0.23	100.52	0.55	74.45	1.34	24.86	37.99	0.00	10.77	11.94	10.36	1.03	2.30
14	1244	5.79	51.08	1.13	18.56	6.42	9.64	10.67	2.75	0.20	100.47	0.58	74.84	1.20	23.29	37.69	0.00	12.24	14.31	8.64	1.04	2.14
16	1239	4.95	51.29	1.03	18.13	6.40	9.84	11.00	2.48	0.18	100.34	0.61	75.28	1.07	20.95	37.81	0.00	13.41	18.60	5.58	1.03	1.96
18	1233	3.96	51.54	0.94	17.68	6.35	10.01	11.33	2.20	0.16	100.22	0.64	75.75	0.97	18.62	37.89	0.00	14.66	22.95	2.39	1.02	1.79
											Initial Melting At 6 kbar											
6	1225	5.84	51.10	1.42	20.42	5.98	8.66	9.50	3.27	0.35	100.69	0.47	74.15	2.04	27.65	40.02	0.00	5.71	11.11	10.56	0.96	2.70
8	1224	5.69	51.21	1.37	20.12	6.01	8.80	9.80	3.19	0.30	100.79	0.49	74.38	1.74	27.01	39.69	0.00	7.14	11.68	10.02	0.97	2.59
10	1222	5.39	51.34	1.29	19.74	6.04	8.98	10.11	3.08	0.26	100.83	0.51	74.66	1.52	26.08	39.25	0.00	8.73	12.72	9.16	0.97	2.46
12	1219	4.92	51.47	1.21	19.30	6.06	9.17	10.43	2.94	0.23	100.81	0.54	74.99	1.34	24.86	38.81	0.00	10.34	14.32	7.92	0.98	2.30
14	1216	4.29	51.62	1.13	18.84	6.07	9.37	10.74	2.75	0.20	100.73	0.57	75.35	1.20	23.29	38.45	0.00	11.87	16.69	6.17	0.98	2.14
16	1211	3.50	51.82	1.03	18.38	6.06	9.56	11.06	2.48	0.18	100.57	0.60	75.76	1.07	20.95	38.50	0.00	13.11	20.96	3.11	0.98	1.96

*Extent of partial melting (F) is in weight percent; †Temperature (T) is in degrees Celsius; and ‡Pressure of final melting is in kilobars. All oxides and normative components are in weight percent. Norms assume 10% of total Fe as Fe_2O_3.

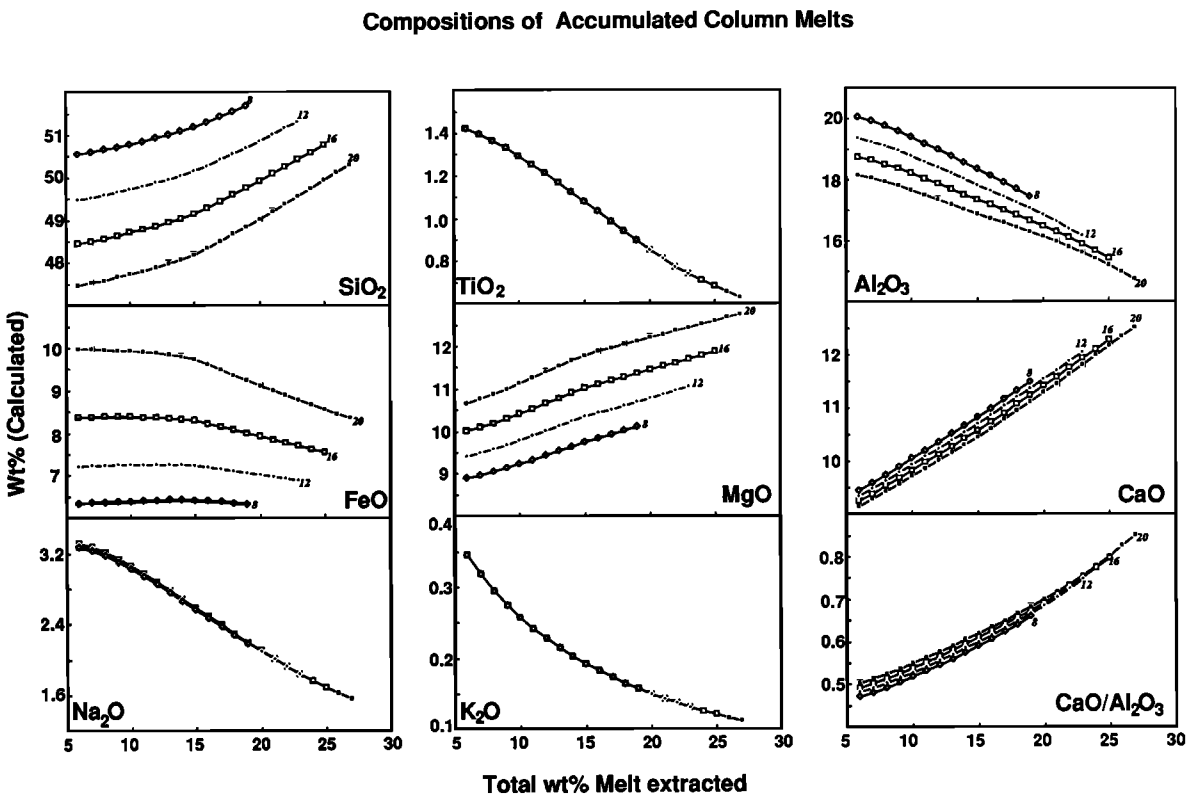

Fig. 10. Calculated compositions of accumulated (pooled) column melts using our empirical model. Data are from Table 6. Small numbers give the initial melting pressures. See text for detailed discussion.

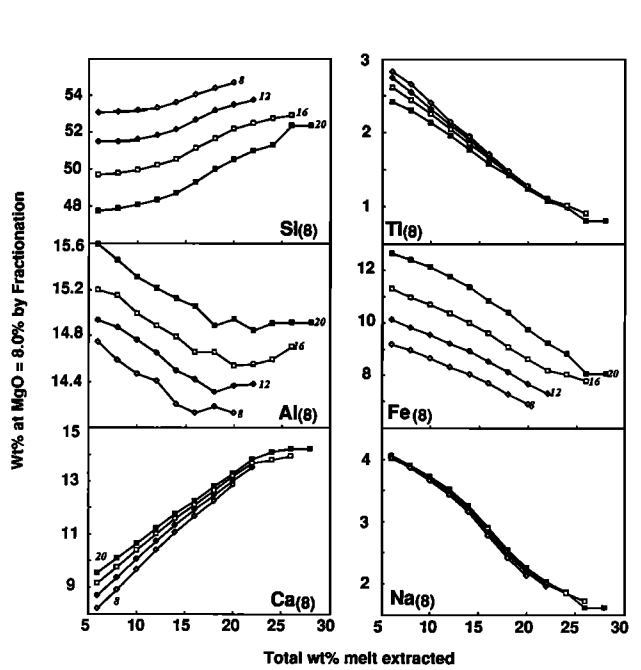

Fig. 11. Compositions in Table 6 fractionated to MgO = 8.0 wt % using low pressure liquid lines of descent program of *Weaver and Langmuir* [1990]. The abundance of each of the oxides at MgO = 8.0 wt% is shown as $Si_{(8)}$, $Ti_{(8)}$, $Al_{(8)}$, and so on. The numbers by the curves represent the initial pressures of melting (P_o = 20, 16, 12, and 8 kbar). See text for discussion.

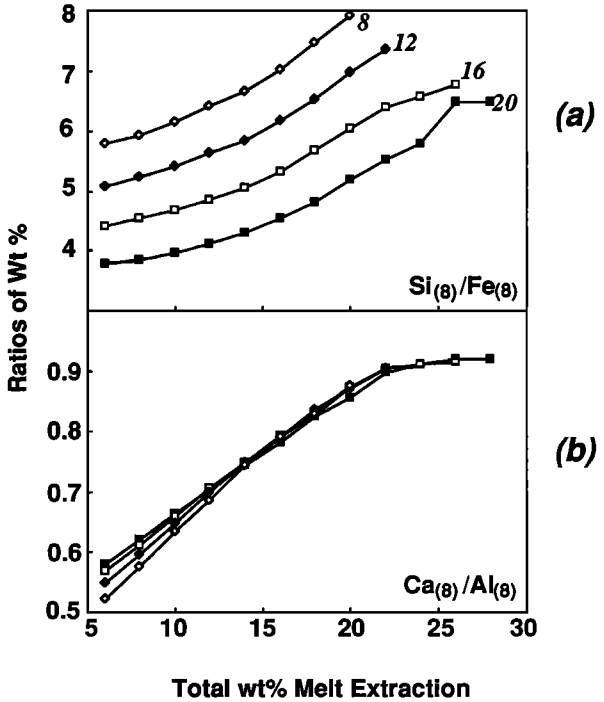

Fig. 12. The (*a*) $Si_{(8)}/Fe_{(8)}$ and (*b*) $Ca_{(8)}/Al_{(8)}$ ratios versus extent of partial melting. These are calculated from the results of Figure 11 for each P_o (20, 16, 12, and 8 kbar as labeled). Note that $Si_{(8)}/Fe_{(8)}$ is very sensitive to pressure, and $Ca_{(8)}/Al_{(8)}$ is almost independent of pressure but strongly dependent on F. See text for discussion.

$$F\ (wt\%) = 19.202 - 5.175\ Na_{(8)} + 15.537\ \frac{Ca_{(8)}}{Al_{(8)}} \qquad (9)$$

Figure 13 shows the linear inverse correlation of $Na_{(8)}$ and $Ca_{(8)}/Al_{(8)}$ for different F with superimposed natural MORB glasses with MgO = 7.8–8.2 wt % from the EPR, MAR, and Indian Ocean (W. G. Melson and T. O'Hearn, personal communication, 1989). Our model indicates that these MORB melts were probably produced by 10–20 % melting, which is consistent with studies of mantle peridotite indicating that the residual mantle contains clinopyroxene [*Dick et al.*, 1984]. Finally, using (5) (and Figure 9), we can derive an expression for the final melting pressure (P_f) at which melting may cease. For this, we merely compute the amount of pressure release required to produce an amount of melt F:

$$P_f\ (kb) = (1.3613\ P_o + 3.9103) + (-1.3458\ P_o - 13.592)/F$$
$$+ (-0.03015\ P_o - 0.2929)F \qquad (10)$$

Note that the (10) assumes adiabatic melting paths. It may not apply if melting occurs in a regime of nonadiabatic thermal gradients. In addition, given the uncertainties in the actual melting path discussed previously, the P_f values are less certain than P_o values. For the simple case of adiabatic column melting considered here, however, (10) is appropriate. The expressions we present for computing P_o, P_f, and F are clearly model dependent. The formal errors in these derived expressions are small (±2% for F, ±1 kbar for P_o and P_f; however, their application to natural MORBs involves several other assumptions (discussed earlier). For this reason, actual uncertainties in application of these expressions are unknown. Nevertheless, because most of the assumptions we have made are probably reasonable, in the next section we apply the model results to natural MORB compositions from three localities: a fast-spreading ridge, a slow-spreading ridge and a chain of near-EPR-axis seamounts.

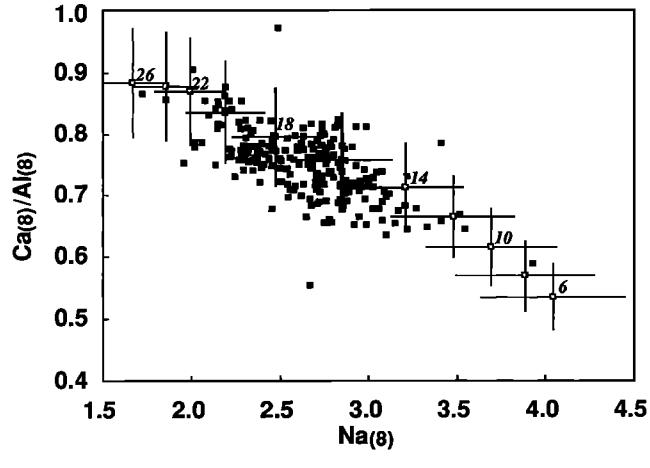

Fig. 13. The correlation of $Ca_{(8)}/Al_{(8)}$ with $Na_{(8)}$ for different extents of partial melting (numbered points). The error bars are derived from the main region of the mantle array analysis of *Falloon and Green* [1987] and show that mantle heterogeneity would not be expected to disturb the observed correlation. We use this correlation to determine the extent of partial melting. We also superimpose 231 natural MORB glasses with MgO = 7.8–8.2 wt% for all oceans from the Smithsonian data base [W. G. Melson and T. O'Hearn, personal communication, 1989] and the JOI Synthesis of the EPR [*Tighe*, 1988]. This indicates that most MORBs result from 10–20% partial melting.

CASE STUDIES

East Pacific Rise: 8°N to 14°N

The East Pacific Rise at 8°N to 14°N has been well studied by *Langmuir et al.* [1986] and *Batiza and Niu* [1989]. Most of the major and trace element data for this portion of the EPR are available in the Joint Oceanographic Institutes (JOI) synthesis of the EPR [*Tighe*, 1988]. We use these data (average sample spacing is < 8 km) and our model to examine patterns of P_o and F. In this analysis, we exclude a small number of samples with MgO < 5.0%, primarily from the 9°03' Overlapping Spreading Center (OSC). First we divide the EPR into seven segments [*Macdonald et al.*, 1988], even though many more chemical segments [*Langmuir et al.*, 1986] could be chosen. For each segment, we derive individual liquid lines of descent and use these to correct for low pressure fractionation (to MgO = 8.0 wt %) within each segment. For smoothing and to remove the effects of very localized chemical changes, we apply a moving boxcar filter to the data. The boxcar has a fixed width of five

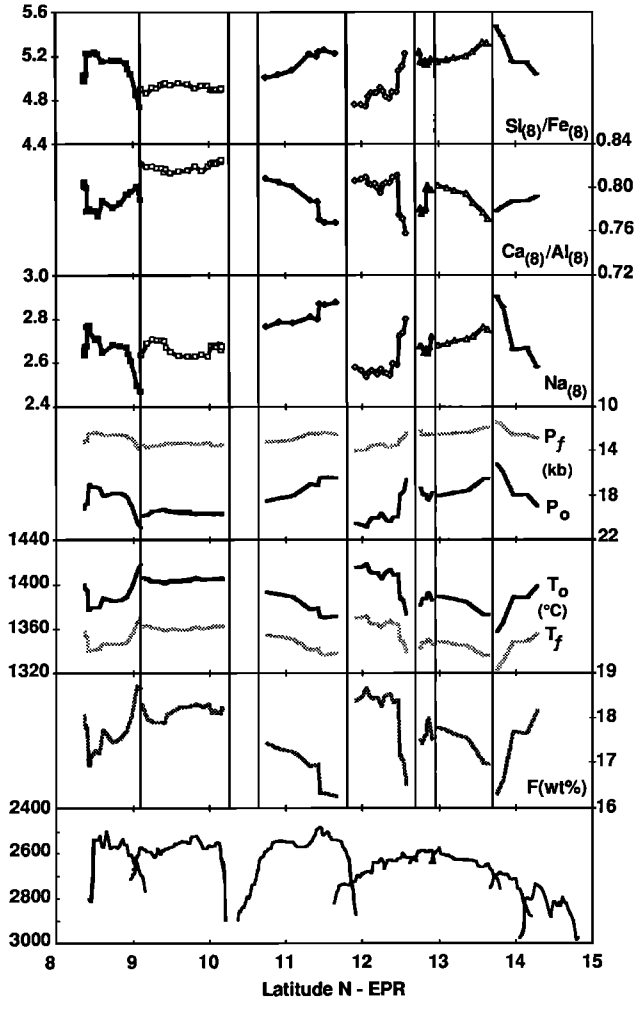

Fig. 14. The East Pacific Rise (EPR) between 8° and 14°N. The bottom panel shows topography [*Macdonald et al.*, 1988] and the other panels show $Si_{(8)}/Fe_{(8)}$, $Ca_{(8)}/Al_{(8)}$, $Na_{(8)}$, and calculated (equations (8), (9), and (10)) initial and final melting pressures (P_o and P_f), the initial and final temperature (T_o and T_f), and the extent of partial melting (F). Note that broad along-axis dome in P_o, T_o, and F between 8°N (Siqueiros transform) and the 11°45'N OSC. Also note the edge effects at OSCs. See text for a full description of the filtering used to produce this figure and interpretations of the results.

continuous dredge locations, except near segment boundaries where it is three dredges wide. The boxcar advances one dredge at a time to produce a moving average. Computed values of $Si_{(8)}/Fe_{(8)}$, $Ca_{(8)}/A_{(8)}$, and $Na_{(8)}$ and calculated P_o, P_f, T_o, T_f, and F are shown in Figure 14 against latitude.

On the basis of our model, MORB melts in this region of the EPR were produced at various initial pressures (P_o) from 15–21 kbar (45–63 km), and extent of melting (F) varying from ~16% to 19%. Edge effects can be seen at several tectonic features, but not all. The Clipperton transform is a notable exception, in agreement with *Klein et al.* [1987]. The edge effects are not consistent; for example, at the 9°03'N OSC, P_o increases toward the OSC, but at the 12°37'N and 13°43'N OSCs and the southern limb of the 11°45'N OSC, P_o decreases toward the OSC. In terms of mantle temperature [*Klein and Langmuir*, 1987; *McKenzie*, 1984], OSCs appear to be mostly underlain by relatively cool mantle, but the 9°30'N OSC is an exception. Some OSCs, such as the one at 12°54'N, show little edge effect in any melting parameter. Overall, there is only a poor correlation between large offsets (transforms and OSCs) and the melting parameters; though some edge effects are present, their magnitude and nature are inconsistent from place to place. This agrees with the findings of *Langmuir et al.* [1986].

Between the Siqueiros and the 11°45'N OSC, there seems to be a broad domal pattern in mantle temperature (T_o) with a broad high-temperature region between 9° and 10°N. This broad thermal dome extends across the Clipperton transform without apparent disruption. In contrast, the region from 11°45' to the Orozco transform, which comprises a broad along-axis topographic dome, shows a complex pattern of mantle temperature. If anything, this pattern indicates a low-temperature region at the apex of the dome, rather than a high-temperature region as might be expected. This perplexing pattern of mantle temperature and the general question of how it might be related to mantle flow are discussed later.

The Mid-Atlantic Ridge at 26°S

The petrology and chemistry of the mid-Atlantic ridge (MAR) at 26°S have been discussed by *Batiza et al.* [1988] and *Castillo and Batiza* [1989]. The morphology and geophysical characteristics of the MAR segment are discussed by D. K. Blackman and D. W. Forsyth (Gravity and tectonics on the mid-Atlantic ridge 25°-27°30'S, submitted to Journal of Geophysical Research, 1991) (Hereinafter Blackman and Forsyth, 1991) and N. R. Grindlay et al.(Morphology and tectonics of the mid-Atlantic ridge (25°–27°30'S) from sea beam and magnetic data, submitted to Journal of Geophysical Research, 1991). Figure 15 shows the raw data, corrected for fractionation to a MgO value of 8.0 wt %, plotted against latitude. Though scattered, there are some general patterns of correlation between topography and major element chemistry. After filtering, as with the EPR data, and plotted against depth, these patterns are evident (Figure 16). Using our melting model, we can interpret these patterns in terms of the melting parameters as in Figure 17.

In contrast with the EPR (Figure 14), there is a good correlation between axial depth and melting parameters such as P_o, T_o, and F. Our model suggests that these MORB melts have a relatively narrow range of P_o (14–16 kbar or 42–48 km) and F (16–18% melting). Approaching the offsets that bound the segment, the extent of melting decreases, and the depth of melting increases. We discuss the possible implications of this pattern later.

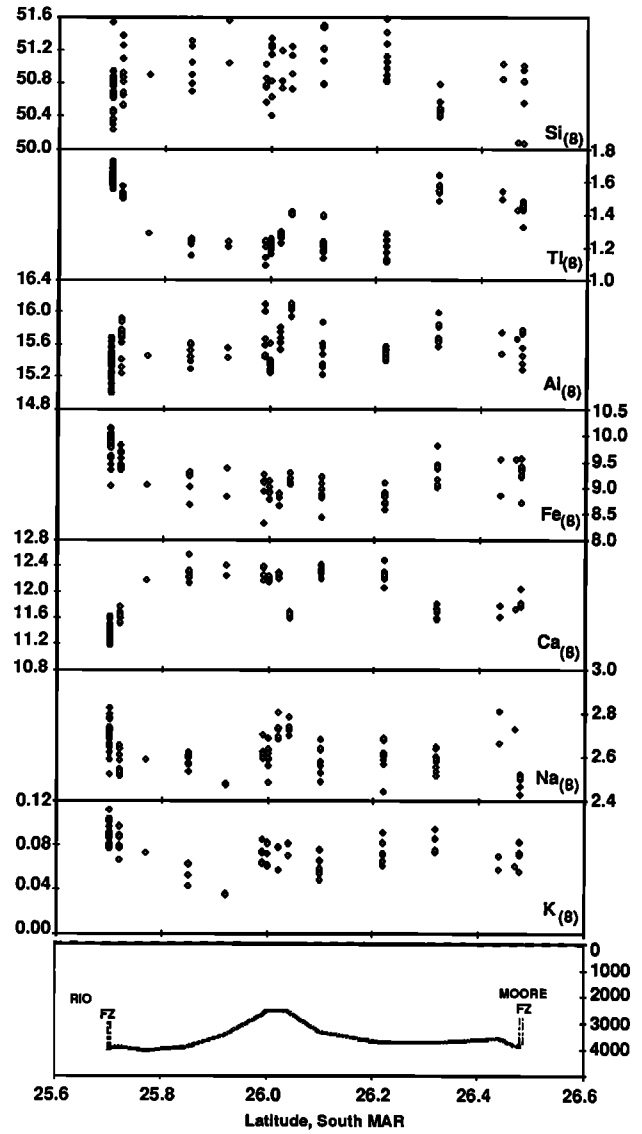

Fig. 15. The mid-Atlantic ridge (MAR) at 26°S from *Batiza et al.* [1988]. The raw data have been corrected for shallow fractionation to MgO = 8.0 wt %. Topography (based on dredging depths) is shown at the bottom.

Figures 18 and 19 show that MORB from the MAR at 26°S show a positive correlation of $Na_{(8)}$ and $Fe_{(8)}$, but an inverse correlation of $Na_{(8)}$ and $Si_{(8)}$. Using the terminology of *Klein and Langmuir* [1989], the MAR at 26°S exhibits the local trend. In contrast, the EPR (8°N – 14°N) displays the global trend even within each segment. This is clearly shown in Figure 20, where we use $Ca_{(8)}/Al_{(8)}$ and $Si_{(8)}/Fe_{(8)}$ as proxies for F and P_o, respectively. In this diagram, as in the work of *Klein and Langmuir* [1987, 1989], the global trend is characterized by an association of increasing depth of melting with more extensive melting. The local trend, in contrast, is characterized by decreasing depth of melting associated with more extensive melting. Using our decompression-induced column-melting model, we can explicitly calculate the slope of the intracolumn trend because this trend simply corresponds to the progressive melting of a mantle parcel undergoing column melting initiated at a single depth (P_o). In Figure 21, we show the calculated column melting variations for the melting paths of P_o = 8, 12, 16, and 20 kbar on $Na_{(8)}$ and $Fe_{(8)}$ and on $Na_{(8)}$ and $Si_{(8)}$

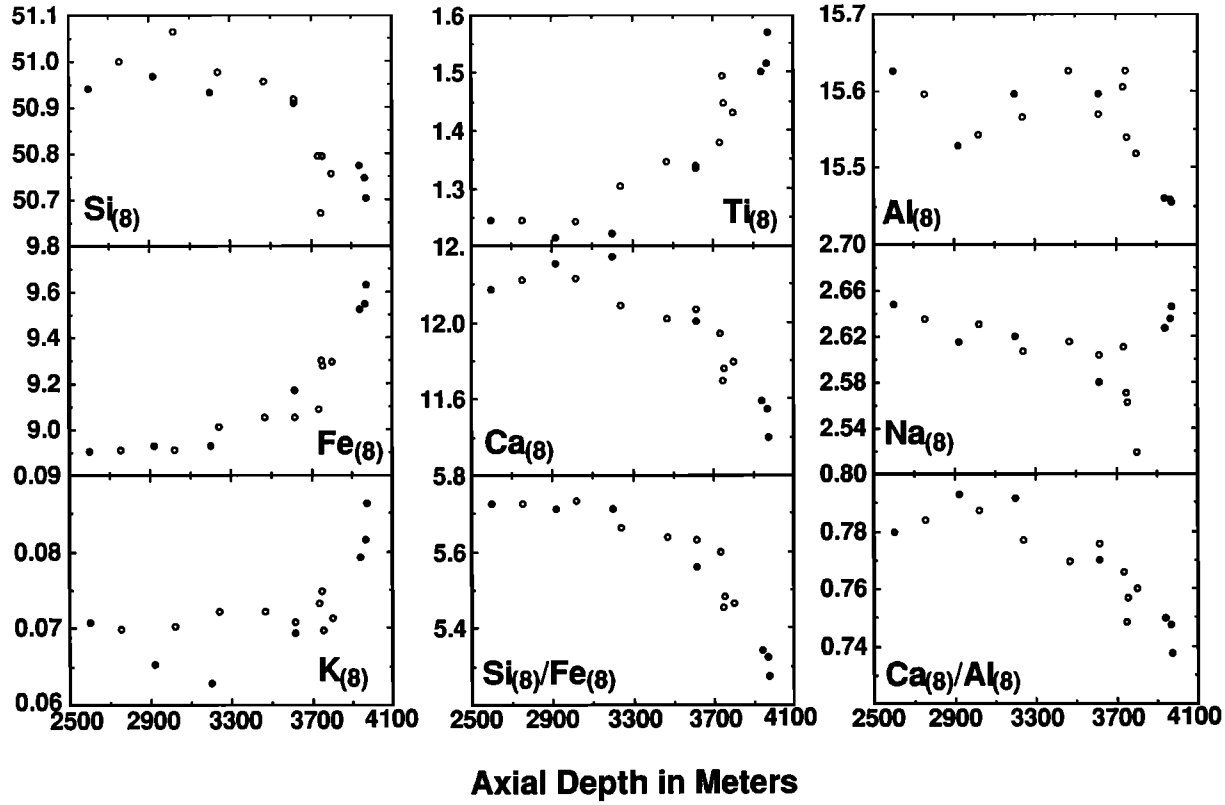

Fig. 16. Filtered data for the MAR at 26°S plotted against axial depth (horizontal axis). Solid circles are points north of the along-axis high, and open circles are points south of the high. Note that most corrected oxide abundances vary with axial depth, particularly for the deep portions of the segment. These results show that extent of partial melting inferred from $Ca_{(8)}/Al_{(8)}$, $K_{(8)}$ and $Ti_{(8)}$ is progressively lower near the offsets (deep portions of the segment). $Na_{(8)}$ does not show a simple pattern, implying that mantle heterogeneity may play some role in this case. $Si_{(8)}$ and $Si_{(8)}/Fe_{(8)}$ indicate that melts near the offsets are produced at greater depths. See text for full discussion.

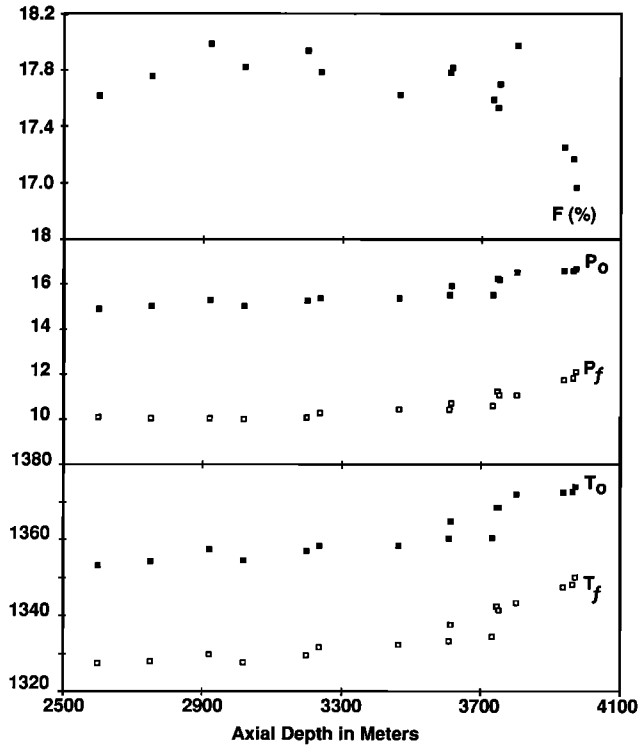

Fig. 17. Calculated extent of partial melting (F) and other physical parameters for the MAR at 26°S plotted against the axial depth. See text for discussion.

diagrams. While the slopes of the intracolumn melting paths are similar in sign to the data from the MAR at 26°S (shown superimposed on Figure 21), the actual slopes differ significantly from each other. We discuss possible interpretations of this difference later.

Near-EPR-axis Seamounts: Lamont Seamount Chain

Batiza et al.[1990] and *Niu and Batiza* [1989] recently showed that young (<1 Ma) seamount chains near the EPR, like the nearby EPR axis, are comprised mostly of zero-age MORB melts. However, near-axis seamounts MORB show systematic chemical differences with EPR axial MORB. As a group, lavas from near-axis seamount chains parallel to absolute plate motion have lower $Fe_{(8)}$ and higher $Na_{(8)}$ than axial basalts. In order to determine whether these changes occur progressively away from the EPR axis along a single seamount chain, we examine a well-studied absolute motion parallel seamount chain. The best studied of these is the Lamont seamount chain [*Fornari et al.*, 1988*a*, *b*; *Allan et al.*, 1989; *Smith and Batiza*, 1989; *Barone and Ryan*, 1990].

Figure 22 shows the chemical variation patterns observed away from the EPR axis along the Lamont seamount chain. Despite some obvious scatter, the patterns are regular and systematic. With our column-melting model, we calculate the melting parameters shown in Figure 23. These patterns suggest a gradual pinching out of the melt zone at 35–55 km off axis. P_o, P_f, and F are relatively constant off axis out to

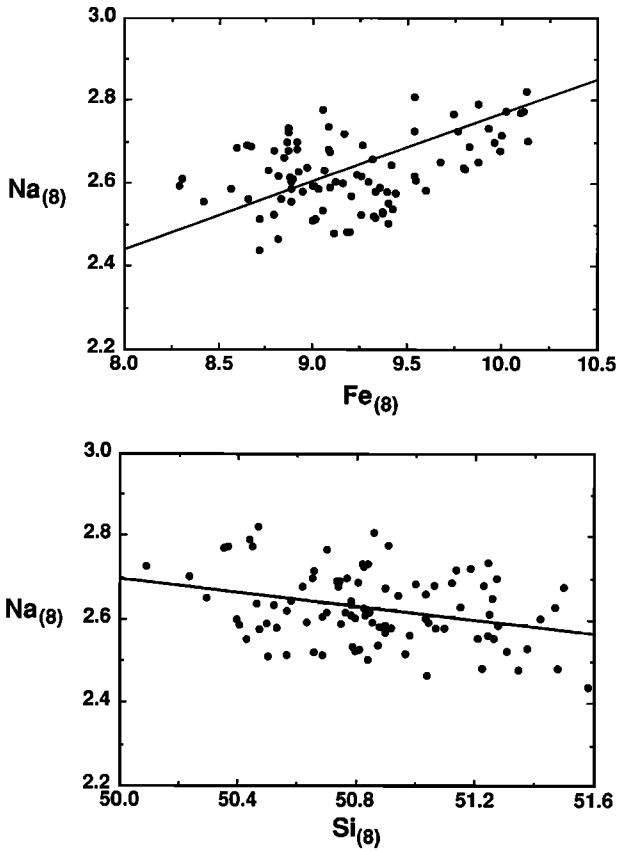

Fig. 18. $Na_{(8)}$ versus. $Fe_{(8)}$ and $Na_{(8)}$ versus$Si_{(8)}$ for MORB from the MAR at 26°S. These correlations represent the local trend of *Klein and Langmuir* [1989].

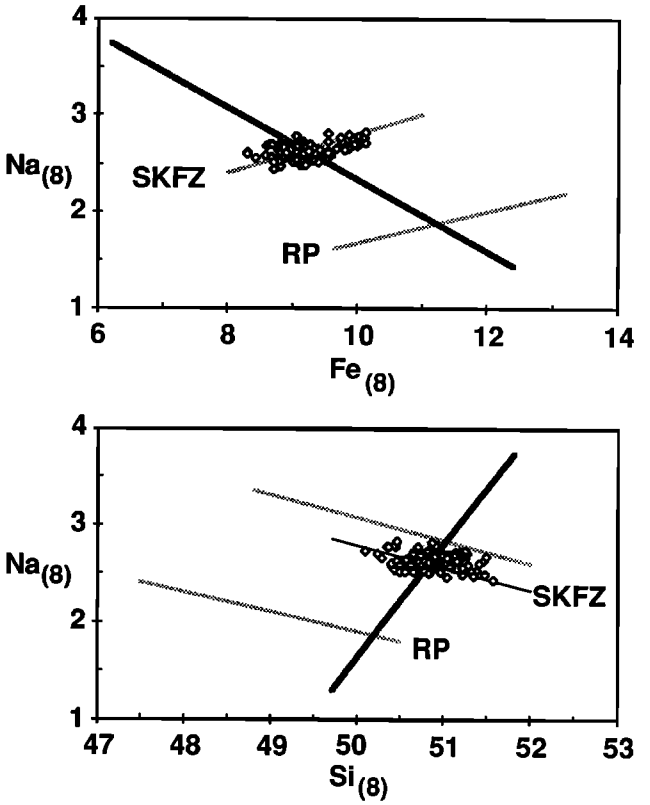

Fig. 19. Same as Figure 18 with the global trend shown as a bold line. The local trend (Reykjanes Peninsula, RP; MAR at South of Kane fracture zone, SKFZ; and MAR at 26°S, open diamonds) crosses the global trend at a high angle.

about 30 km, but at greater distances, P_o shallows, and F decreases. This pattern of shallow, less extensive melting is similar to that observed at many OSCs along axis (see Figure 14) and is opposite to the edge effect at 26°S MAR where decreases in F are accompanied by deeper melting. The axial and off-axis melting region under the Lamont seamount chain is shown diagrammatically in Figure 24.

The Lamont seamount chain is highly depleted in very incompatible elements. For example, $(La/Sm)_N$ in the seamount lavas is systematically lower than at the EPR axis [*Allan et al.*, 1989]. This systematic depletion is interesting because it is opposite to what would be expected for an enriched plume or hot spot that might explain the absolute plate motion orientation of the chain. One possible explanation of the systematic depletion in incompatible elements is that it represents progressive depletion of a source due to continuous melting as upwelling mantle turns to move laterally away from the EPR axis. However, the signature of progressive melting should also appear in the major element melt compositions, but it does not. Another possibility is that the trace element signatures are affected by lateral melt migration toward the EPR axis, as envisioned by *Phipps Morgan* [1987]. In this scenario, the Lamont seamount melts would not strictly represent pooled or accumulated column melts. Instead, they would be pooled melts without the first few percent of melt which might be removed by lateral melt migration.

To test the hypothesis, we calculate the trace element abundances for melts generated by continuous melting. We used equations rederived from *Maaløe* [1982] for critical melting and varied the fraction of interstitial melt (w_o) present during continuous melting. We found that accumulated melt compositions produced in this manner do not correspond to those observed at the Lamont seamounts. However, we can produce very depleted melts as instantaneous melts (versus accumulated melts) produced by continuous column melting. Figure 25*a* shows the results of several calculations. The EPR axial melts are produced by high degrees of partial melting and

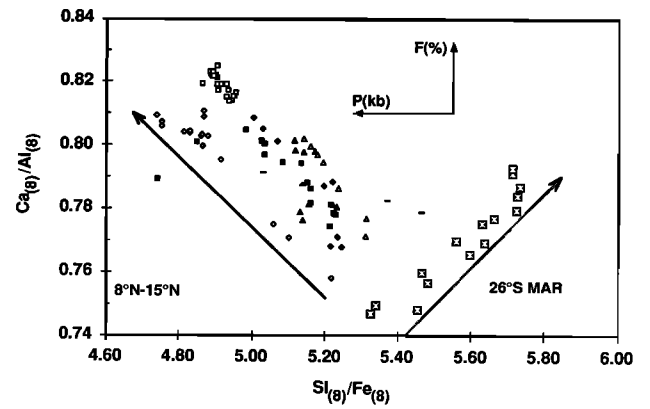

Fig. 20. A more sensitive plot distinguishing the global trend and local trend: $Ca_{(8)}/Al_{(8)}$ versus. $Si_{(8)}/Fe_{(8)}$ diagram, using our data for the MAR at 26°S (local trend) and the seven EPR segments (8°–14°N) (global trend). Note the opposite correlations of the extent of partial melting with the melting pressure for the two trends. Also note that the global trend applies to the entire length of EPR we studied as well as to individual segments (denoted by different symbols), and that no local trend is seen at the EPR.

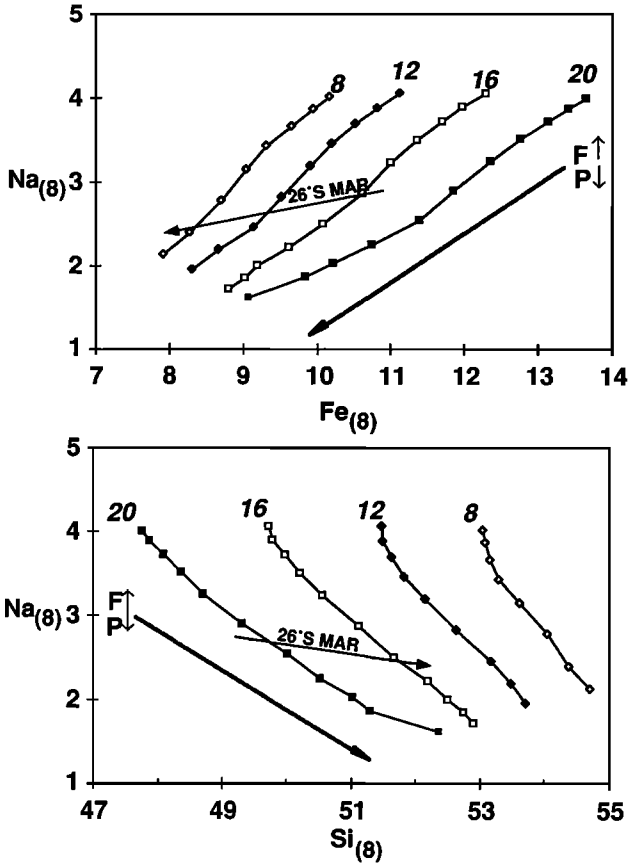

Fig. 21. As in Figure 18, calculated intracolumn (at specified P_O values) melts generated by initial melting at four pressures (20, 16, 12, and 8 kbar). Also shown is the local trend for the MAR at 26°S. Note that the local trend and the intracolumn melt variations are not parallel; thus intra-column melting alone cannot explain the local trend.

melt pooling. The more depleted seamount melts are produced as instantaneous melts from a source similar to that of the EPR ($(La/Sm)_N = 0.55$) at smaller extent of melting and smaller w_o with the first few percent of melts lacking (melt migration ?).

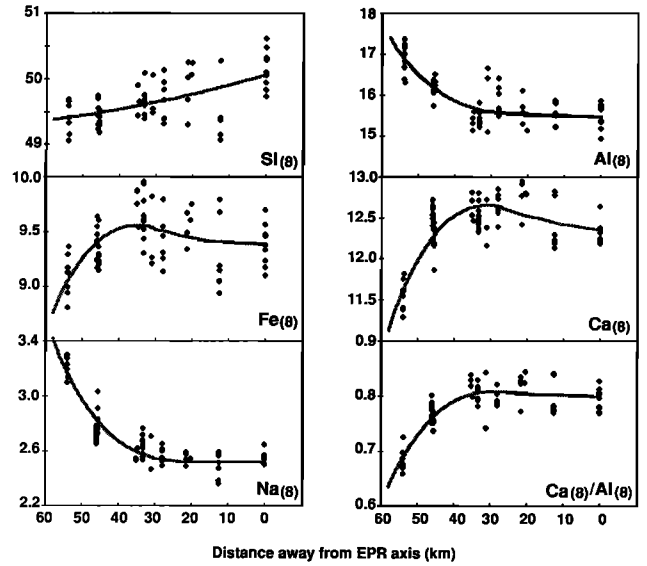

Fig. 22. Chemistry of the Lamont seamount and EPR plotted against distance (kilometers) from EPR axis. Shown are samples with MgO > 8.0 wt % from *Allan et al.* [1989] plus some of our unpublished Raitt 02 data. Heavy lines are calculated model compositions discussed in the text.

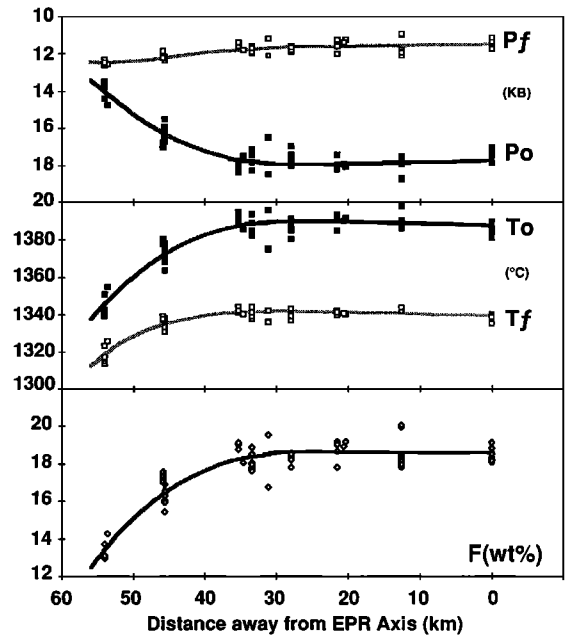

Fig. 23. Calculated column-melting parameters for the Lamont seamounts. Shown are extent of partial melting (F) and initial and final melting pressures and temperatures (P_O, P_f, T_O, T_f). Note that the melt zone pinches out away from the axis.

The good fit of the Lamont trace element data to instantaneous melts may indicate that the Lamont seamounts tap instantaneous melts rather than pooled melts. This is consistent with the hypothesis that the seamount melts are primarily supplied by dikes which tap small amounts of melt. This is also consistent with lateral melt migration which would hinder efficient pooling of melts produced in a rising vertical column. On the other hand, the major elements can be successfully modeled as pooled melts and less well modeled as instantaneous melts. Thus we infer that lateral melt migration toward the axis may play some role, but the magnitude is probably small. Furthermore, if lateral melt migration is the explanation, the pattern of this migration is not simple. A simple pattern of melt migration and tapping of instantaneous melts would result in a regular pattern of $(La/Sm)_N$ decrease away from the axis. Figure 25*b* shows that such a pattern is not observed. The geographic scatter of $(La/Sm)_N$ could result

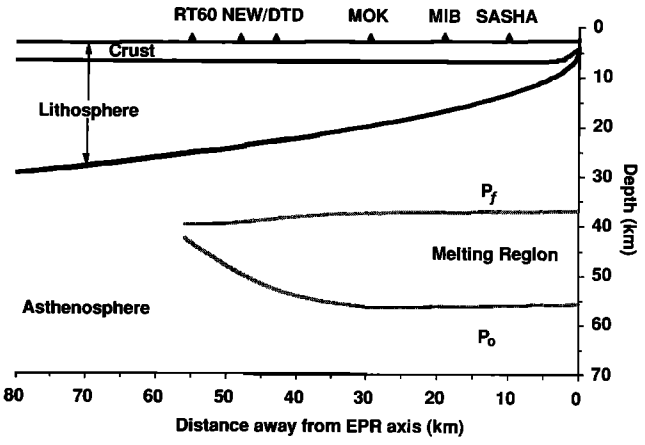

Fig. 24. Diagrammatic presentation of the results in Figure 23 showing the inferred region of melting in the vicinity of the EPR. RT60 is a lava field west of the NEW/DTD seamounts.

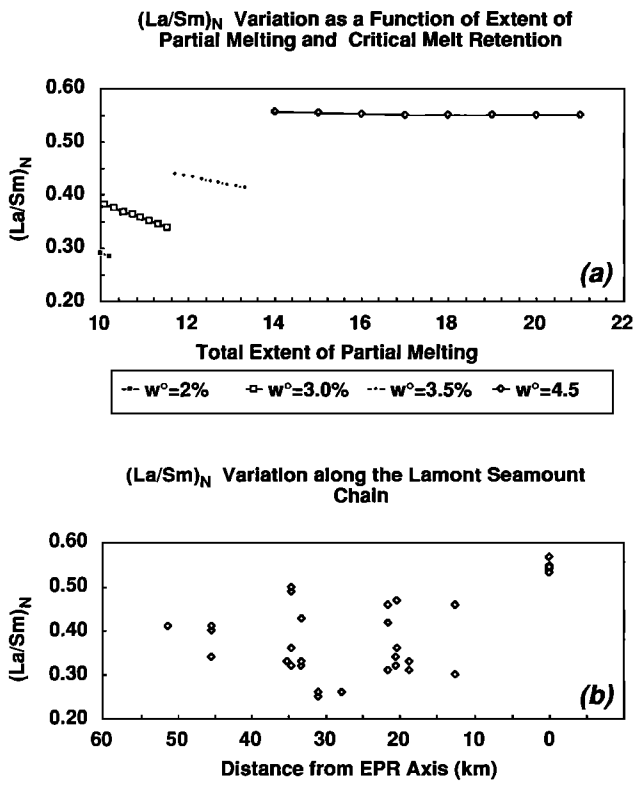

Fig. 25. (*a*) Continuous melting model calculations for very depleted melts of the Lamont seamount chain and the EPR. Melts with $(La/Sm)_N$ = 0.55 are pooled melts (axis), whereas more depleted melts are instantaneous melts produced by column melting with various melt porosities (w_o). (*b*) The $(La/Sm)_N$ for the Lamont seamounts do not show a simple off-axis trend. See text for discussion.

either from a complex pattern of lateral melt migration and tapping or from that fact that all seamount lavas are not of truly zero age [*Barone and Ryan*, 1990]. On the basis of the calculations illustrated in Figure 25*a*, we speculate that lateral melt migration toward the EPR has played a role in producing the trace element depletion of the Lamont lavas. We note, however, that other explanations such as small-scale mantle heterogeneity [*Fornari et al.*, 1988*b*] or complex segregation/mixing scenarios [*Langmuir et al.*, 1977] cannot presently be ruled out.

Discussion

In this section, we discuss the results of our model and some of the possible implications for subaxial magmatic processes that arise from applying the model to fast ridges (EPR), slow ridges (MAR), and near-EPR seamount chains.

Nature of Primary Magma

The debate over the nature of primary magma parental to MORBs has been active for over 20 years [*O'Hara*, 1968; *Green et al.*, 1979; *Stolper*, 1980; *Jaques and Green*, 1980; *Elthon and Scarfe*, 1984; *Falloon and Green*, 1987, 1988; *Presnall and Hoover*, 1984; *Fujii and Scarfe*, 1985; *Fujii and Bougault*, 1983] and is largely based on the interpretations of isobaric batch melts produced in the laboratory and on the use of simplified phase diagrams. As discussed by *Klein and Langmuir* [1987], if MORB is produced by polybaric column melting, not by isobaric batch melting, then the conflicting views may be reconciled. In Figure 26, we plot out model melts (both isobaric batch melts and polybaric column melts for comparison) on the Ol-Cpx-Qtz normative projection of *Walker et al.* [1979]. Also shown are pseudoinvariant points from *Stolper* [1980]. Figure 26*b* shows that for polybaric column melts, the initial melting pressure (P_o) as well as the extent of melting (F) controls the position of a melt composition in this projection.

In Figure 27, we plot natural MORB melts with MgO > 8.5 wt % and also our polybaric column melt compositions fractionated to 8.0 wt % MgO. The good agreement between high-MgO natural MORB and our calculated melts provides additional support for the notion that most MORBs are not primary melts. However, our primary melts have only 10–12 wt % MgO and are not picritic. Our model suggests that most MORBs are generated by initial melting at 12–21 kbar and 10–20 % melting. The melts with 8.0 wt.% MgO can be derived from these primary melts by variable amounts of olivine and plagioclase fractionation at lower-pressure. We thus concur with the view that many MORB melts with 10–12 wt % MgO are primary [*Bryan et al.*, 1981]. The global correlation by *Klein and Langmuir* [1987] strongly supports the idea that

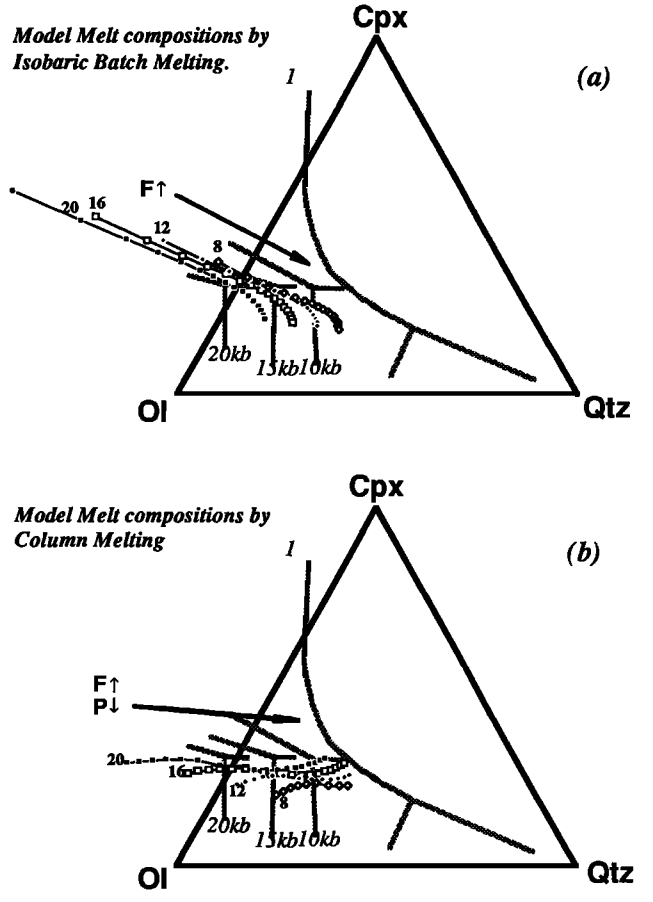

Fig. 26. Normative projections (Cpx-Ol-Qtz from Plagioclase) of calculated partial melts produced by (*a*) isobaric batch melting, and by (*b*) polybaric column melting. The projection algorithms are taken from *Walker et al.* [1979]. High-pressure phase boundaries are from *Stolper* [1980]. In Figure 26*b*, the isobaric melting pressures are 20, 16, 12, and 8 kbar as labeled with extent of partial melting from 10% to 40% in the directions shown by the arrow. Except for high F (Qtz-rich) melts, all the melts should be in equilibrium with three phases (Ol-Opx-Cpx). b). the compositions of accumulated polybaric column melts at the initial melting pressures P_o = 20, 16, 12, and 8 kbars (as labeled) are shown with the arrow indicating decompression and the increasing melt extraction (1% step). Projected melt compositions are from 10% to 26%, 24%, 22%, and 20% for the initial pressures respectively. Data are from Table 6 and Figure 10.

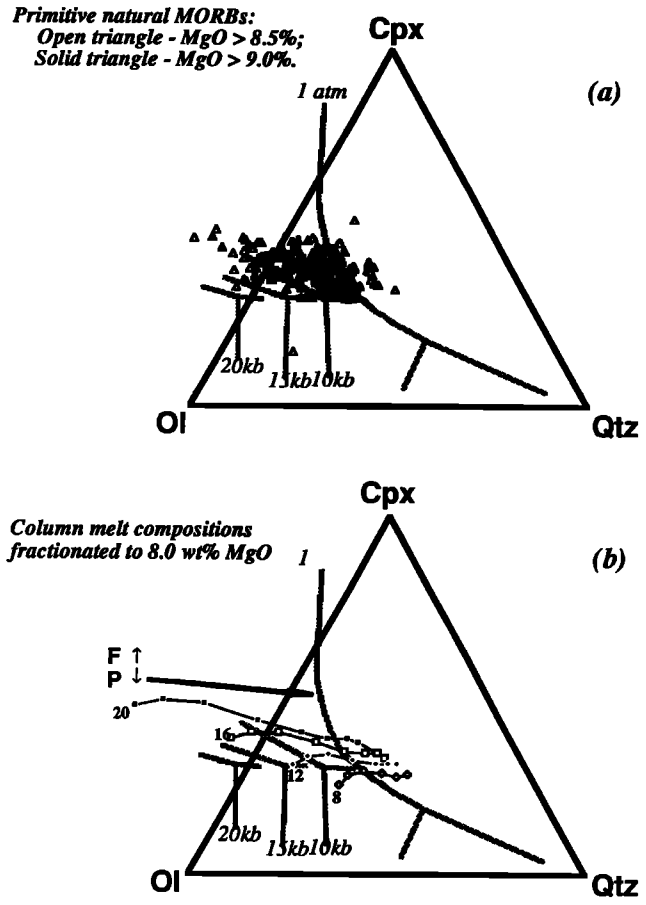

Fig. 27. As in Figure 26: (*a*) primitive MORBs with MgO > 8.5% (open triangles) and MgO >9.0% (solid triangles) from the EPR, MAR and mid-Indian ridges from the Smithsonian data base (W. G. Melson and T. O'Hearn, personal communication, 1989); and (b) the fractionated compositions in Figure 26*b* with 2% steps for each of melting paths (P_o = 20, 16, 12, and 8 kbar as labeled). This comparison shows that the majority of observed MORBs are fractionated at low pressure from the melts accumulated during column-melting process with initial melting pressures ranging from 12 to 21 kbar and with the total melt production ranging from 10 to 20 wt %.

mantle temperature and column-melting processes control the composition of MORB melts. As shown by many previous studies, shallow fractionation is also an important process for most observed MORB compositions. Clinopyroxene-dominated fractionation at high pressure apparently plays a minor role, since this would tend to deplete SiO_2 in liquids and would lead to different fractionation patterns than those shown in Figure 27*b*.

Mantle Temperature Distribution and Upwelling

The major element chemistry of MORB melts provides a very strong (via experimental studies) constraint on the temperature of the mantle. Though somewhat model dependent, this is probably the strongest direct constraint on mantle temperature available. We thus discuss the mantle temperature variation we infer from the application of our melting model to natural MORBs. While most physical models of mantle upwelling assume that the subaxial mantle has constant potential temperature (i.e., adiabatic temperature profile) and horizontal isotherms (Figure 28), we find strong evidence for significant lateral temperature differences (up to 60°C) occurring on a scale of 50–100 km. If these differences are real, their cause is important, because mantle temperature and upwelling in some cases are related. We discuss lateral temperature gradients observed both along axis and across axis.

Across-axis temperature variation. The across-axis temperature pattern shown by comparing axial chemistry and young (<1Ma) near-axis seamounts indicates that the mantle is cooler away from the axis than directly below the axis. There can be little doubt that this pattern is real, as it is revealed by large groups of seamount samples [*Batiza et al.*, 1990] as well as individual seamount chains such as the Lamont seamount chain (Figure 23). This pattern of P_o and T_o (the solidus temperature and pressure), though perhaps not surprising, contradicts the assumption of horizontal isotherms in the mantle commonly assumed in simple physical models of sub-axial flow. One possibility is that this temperature difference is fortuitous and simply reflects thermal heterogeneity in the upper mantle. Such patterns could perhaps result from compositional heterogeneity and differences in thermal conductivity or stress [*Yoder*, 1976]. However, because of the widespread occurrence of this phenomenon along the EPR [*Batiza et al.*, 1990], this seems highly unlikely.

Another possibility is that small scale convection [e.g., *Buck and Parmentier*, 1986; *Scott and Stevenson*, 1989; D. Scott, personal communication, 1990] might cool the mantle

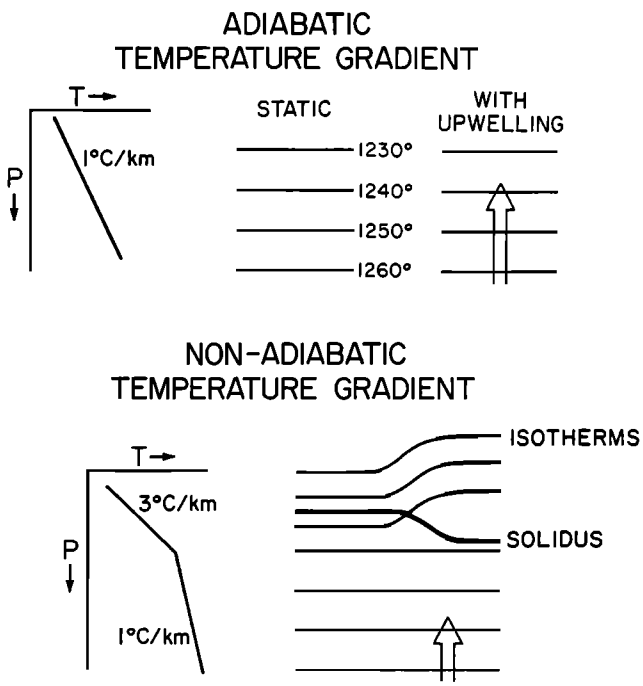

Fig. 28. Schematic diagram of how upwelling (arrow) in a nonadiabatic thermal gradient can affect the patterns of isotherms and the depth of initial melting. For the adiabatic case, upwelling does not perturb the pattern of isotherms because all the material has the same potential temperature [*McKenzie*, 1984; *McKenzie and Bickle*, 1988]. However, if cooling occurs (by any process) and the gradient is larger than adiabatic, upwelling material (arrow) adds heat to this region. This raises the pattern of isotherms and causes lateral temperature gradients. In addition, the hot upwelling material will have a higher temperature than the static material at depth. It will thus melt at a higher temperature and pressure if it continues to rise adiabatically. Steepness of the lateral thermal gradients is controlled by the vigor of upwelling and the size of the nonadiabatic geotherm.

below the lithosphere adjacent to the axis. This cooling would allow upwelling patterns of hot mantle to cause a lateral thermal gradient as shown in Figure 28. A problem with this hypothesis is that for such a condition to be initiated, the residual mantle emplaced across axis by flow must cool a great deal to become denser than hot, fertile mantle near the axis [e.g., *Sotin and Parmentier*, 1989; *Niu and Batiza*, 1991; L. Fleitout, personal communication, 1991]. This cooling would be expected to take tens of millions of years, so small-scale convection very near (30–50 km) the axis may be difficult. Even so, it may not be possible to completely rule out this possibility. At any rate, any conductive or convective process operating below young lithosphere could produce the observed pattern.

Another possibility that can be considered is that the actual temperature gradient in the mantle below the ridges is slightly greater (cooler) than adiabatic for young lithosphere. An adiabatic profile is assumed below the cooling plate, which is the upper conductive boundary layer [*McKenzie and Bickle*, 1988]. However, even a small amount of conductive cooling in the asthenosphere directly underlying the lithospheric plate would make the geothermal gradient greater than adiabatic, as in the thermal boundary layer for old lithosphere proposed by *McKenzie and Bickle* [1988]. Such cooling near the boundary might be explained by long-term (10^7 years) physical proximity between the plate and the underlying asthenosphere. Since ridges are not fixed relative to the underlying mantle, this asthenosphere, with a weak conductive geotherm could be tapped by a ridge axis. If upward flow beneath the axis is partly driven by buoyant forces (not merely plate separation), and if this mantle upwells adiabatically, then upward mantle flow would result in hot rising mantle material being emplaced next to cooler mantle at the edge of upwelling (Figure 28). The most vigorous buoyant upwelling in the core of the upwelling zone would be hottest because this material rises adiabatically from a deeper level within the zone characterized by a weak conductive (versus convective or adiabatic) thermal gradient. This effect would be expected to grade outward from the core of the upwelling toward the edges and would establish a lateral thermal gradient of the type observed. This effect probably need not be dramatic to produce a lateral temperature gradient of 50°–70°C over a distance of 30–50 km away from the axis.

Because of the potential difficulties with small-scale off-axis convection rolls, we favor this explanation for the observed lateral temperature gradient near the EPR. If correct, this implies that some component of buoyant upwelling may occur beneath the EPR, even if in general, the upwelling pattern is mainly controlled by plate separation (*Lin and Phipps Morgan*, 1991).

Along-axis temperature variation. Figure 14 shows small-scale, along-axis temperature differences of 40–50°C below the EPR. Whatever the cause of these variations, one might expect these differences to be related to upwelling flow patterns because if the composition is constant, hotter mantle would be less dense and less viscous than cooler mantle. One might even expect mantle temperature patterns and upwelling to correlate with topography along the EPR [e.g., *Macdonald et al.*, 1988]. Of course this would not necessarily be the case for flow driven exclusively by plate separation if the mantle geotherm is adiabatic.

The broad dome in T_o between Siqueiros transform and 11°45'N OSC (Figure 14) may indeed be a broad, along-axis upwelling. If so, a component of buoyancy-driven flow and/or a weakly conductive thermal gradient like that discussed earlier would be expected to play a role. The edge effects at OSCs, most prominent north of the 11°45'N OSC (see Figure 14), are difficult to explain. One possibility is that southward propagation of the OSCs [*Macdonald et al.*, 1987] places the new limb of the OSC slightly off center from the main upwelling zone. In this case, as for the off-axis cooling documented by seamounts, the mantle material which finds itself below the newly extended ridge could be cooler than normal. In contrast, a portion of ridge that is stable (not propagating) would be expected to establish a robust passive upwelling supply centered directly underneath the axis. This stability could also be perturbed by lateral migration of the ridge away from established upwelling.

Although filtered to suppress local chemical variations, the patterns of Figure 14 provide no evidence for the existence of upwelling patterns linked to small-scale tectonic segmentation. Such patterns would not necessarily be reflected as temperature anomalies. However, since the EPR data are consistent with the global trend in pressure-melting relationship, the upwelling pattern should be reflected in the patterns of T_o. On the basis of gravity and morphology (*Lin and Phipps Morgan*, 1991), it seems most likely that upwelling is curtain like and mainly driven by plate separation. Thermal perturbation in this curtain flow, however, could add a component of buoyancy-driven upwelling such as may exist between Siqueiros transform and 11°45'N OSC. Superimposed on this, a hierarchical series of small perturbations could also be present [*Langmuir et al.*, 1986; *Macdonald et al.*, 1988] though the mantle temperature signal of the small features could be small to nonexistent.

In contrast with the EPR, the MAR at 26°S displays a much different pattern of lateral temperature variations and melting. The slightly smaller extent of melting seen at the offsets of the 26°S segment (Figure 17) may be consistent with the model of *Phipps Morgan and Forsyth* [1988] for subdued upwelling under transforms. However, the higher temperatures are not consistent with this model, though the temperature differences along the segment are small (30°–40°C). It is possible that the calculated temperature pattern of Figure 17 is an artifact resulting from the failure of assumptions in our model. For example, the major element compositions of the mantle may be heterogeneous beneath this ridge segment. The scatter of Na_2O and Al_2O_3 (Figure 16) may favor this notion, but the systematics and correlations of most of oxides and ratios, particularly K_2O and TiO_2, indicate that mantle heterogeneity alone is probably inadequate to explain the results. If K_2O and TiO_2 are used to evaluate the extent of melting, then the F pattern in Figure 17 would be even more pronounced, i.e., the melting column approaching offsets would be even shorter than indicated in Figure 17. If mantle heterogeneity were the cause, then it would be fortuitous for such heterogeneity to be distributed symmetrically about the central topographic high.

Our model implicitly assumes that melts rise vertically to the surface. Thus if significant lateral along-axis melt migration of the type proposed by *Phipps Morgan and Forsyth* [1988] occurs, our model would be invalid. Given the regular chemical variation patterns with depth along axis and the fact that intracolumn melting cannot completely explain the chemical patterns, significant melt migration seems unlikely; however it cannot be ruled out. We also cannot rule out age differences among the axial lavas. If significant age differences occur, then the inferred patterns of T_o need not

represent a steady state or snapshot of thermal conditions. Instead, the pattern would be a mixture of conditions existing at different time.

This segment shows a bull's-eye pattern of gravity (Blackman and Forsyth, 1991), thus the focused buoyant upwelling mantle of *Lin et al.* [1990] and *Lin and Phipps Morgan* [1991] might be expected to apply. However, there is no evidence in the melting patterns or inferred thermal structure for such a pattern. One possibility is that the geotherm under the segment is adiabatic, in which case the upwelling pattern would not disturb isotherms, and the solidus depth (P_o) and temperature (T_o) would be unaffected. This may be the case, but it does not explain the higher T_o under the offsets, which our prior arguments would say is indicative of more vigorous, not less vigorous, upwelling. Perhaps frictional heating occurs within the transform; however, it is difficult to imagine how such heat could be transported to deeper levels of the asthenosphere.

Width of the Upwelling Zone Beneath the EPR

Volcanically active seamounts exist up to 50–60 km from the EPR axis, providing clear evidence that the zone of upwelling is ~100 km wide as proposed by *Phipps Morgan* [1987]. However, because of the across-axis temperature differences discussed earlier, we also suggest that even though the passive, plate driven upwelling zone is wide, much or most of the mantle flux may actually be confined to a narrow central zone of high-velocity upwelling partly controlled by compositional, melt, and thermal buoyancy. This would explain both the across-axis and the along-axis temperature variation patterns discussed earlier, but it requires a weakly conductive versus adiabatic temperature profile.

Global Trend Versus Local Trend

Klein and Langmuir [1987] discovered the global correlation of MORB chemistry with ridge axial depth based on segment-averaged data and successfully explained the origin of this correlation with a simple column-melting model. *Brodholdt and Batiza* [1989] independently compiled unaveraged data and confirmed this correlation, but they show great scatter about the global correlation. *Klein and Langmuir* [1989] found that the scatter partly results from regional scale chemical variations of the type found by *Batiza et al.* [1988] which show opposite correlations to the global trend. They called the global correlation the global trend and the regional scale correlation the local trend in diagrams such as Figures 18 and 19. They explained the global trend by intercolumn melting by assuming a single column represents a segment or locality within which chemistry is averaged. In contrast, they interpreted the local trend as produced by melts tapped from different depths within a single column (intracolumn melting). This study quantitatively confirms their interpretation of the global trend, characterized by a positive correlation of melting pressure with extent of partial melting as represented by 8°N–14°N EPR (Figure 20). In the case of the EPR, however, there does not exist an obvious correlation with axial depth that may be related to the crustal thickness [*Klein and Langmuir*, 1987]. Partly, this may be because the overall topographic relief is relatively small (<400 m) at the EPR and the melting parameters vary in a narrow range. Nevertheless, the global scale correlations of MORB chemistry with ridge axial depth discovered by *Klein and Langmuir* [1987] are clearly evident.

As shown previously, however, the local trend is more problematic. Intracolumn-melting processes produce similar, but not identical, data arrays as the local trend. As noted by *Klein and Langmuir* [1989], the local trend appears to be confined to slow spreading ridges like the MAR. Kinzler and Grove (1991) propose that the local trend is the result of high-pressure fractionation. If so, why does such fractionation only occur at slow-spreading ridges? Perhaps the depth and mechanism of eruption/intrusion vary systematically with spreading rate [*Klein and Langmuir* 1989].

Since the MAR at 26°S displays the local trend, it may shed light on the cause of the local trend. Earlier we concluded that mantle heterogeneity, lateral melt migration, or temporal variability in axial lavas could help explain the perplexing P_o and T_o patterns below this segment. If so, then each or any of these must vary as a function of spreading rate. We speculate that the local trend is in fact due to the dynamics of melt supply, as did *Klein and Langmuir* [1989]. *Lin and Phipps Morgan* (1991) provide strong evidence that the dynamics of upwelling change as a function of spreading rate. We suggest that at the MAR 26°S, melting columns are shorter and deeper at offsets, perhaps owing to a cold-edge effect at shallow levels. By contrast, in the center of the segment, melting columns are longer. If P_o varies and if the multiple melting columns within a segment overlap significantly in their melting range (ΔP), then groups of aggregate column melts might be expected to yield data arrays that are intermediate in slope between intercolumn and intracolumn melting, as observed for the MAR at 26°S.

Geometry of the Melting Region

Application of our model to both axis and seamount melting processes shows that mantle melting actually occurs in a thin layer that pinches out laterally away from ridge axis at distances of 50–60 km in the case of EPR. The thickness of the layer, defined by ΔP (P_o - P_f), varies from 15–30 km. Equation (10) assumes a perfect adiabatic column melting process, and the calculated values of P_f are likely the maximum in practice if the case is nonadiabatic. If, as we suggest, the compositional effect on melting behavior is such that column melting is buffered at the solidus of a progressively depleted source, the melting could stop at a greater depth than calculated P_f. An important constraint on the final depth of melting is provided by crustal thickness, if little melt is retained in the mantle residue.

Crustal Thickness and Melt Migration

Our decompression-induced column-melting model allows us to crudely calculate crustal thickness as the product of the melting interval (P_o - P_f) and the melt fraction with pressure-related density corrections [*Niu and Batiza*, 1991]. Rough crustal thicknesses for the EPR and the MAR derived in this manner are slightly low, but still quite reasonable considering the model uncertainties. We obtain crustal thicknesses which vary from 2.70 to 5.01 km (with a mean thickness of 4.02 km). Our crustal thicknesses are lower than those of *Klein and Langmuir* [1987] partly because our melting interval (P_o - P_f) is shorter than theirs (P_o to the base of the crust). Given the uncertainties in the exact shape of the melting region, upwelling rate of melting mantle, melt migration, and melt retention processes, it is difficult to construct a good mass balance for melt in the crust and mantle. Hopefully, future

additional constraints will provide better estimates of actual crustal thickness and the melt budget. The difficulty of making a melt budget hampers direct tests of the importance of steady state lateral melt migration. While interpretation of the trace element data for the Lamont seamounts provides weak evidence for such possible migration, this suggestion is somewhat speculative.

CONCLUSIONS

From this study, we draw the following conclusions. (1) The experimental data of *Jaques and Green* [1980], *Falloon et al.* [1988], and *Falloon and Green* [1987, 1988] provide a good basis for a distribution coefficient based melting model. The data are self-consistent, and our model for isobaric batch melting yields very reasonable quantitative results. (2) Our decompression-induced column-melting model can be used to calculate melt compositions produced by column melting of peridotite MPY-90. Since this is a reasonable parental composition for MORB, we are confident in applying the model to natural MORB compositions. A possible shortcoming of our model is the assumption that the oceanic mantle beneath mid-ocean ridges is homogeneous with respect to major elements. Thus, we suggest that the coefficients in Tables 4 and 5 should be adjusted if the mantle source composition can be determined independently for any desired specific case study. (3) Application of our model suggests that most MORBs are derived by decompression-induced column melting initiated at depths of 12–21 kbar (40–65 km) and 10–20% melting. Primary column melts for most MORBs have MgO = 10–12 wt %, so most MORBs have undergone some fractionation. We suggest that this fractionation occurs mostly at shallow level. (4) We find that $Si_{(8)}/Fe_{(8)}$ is a sensitive chemical indicator for melting pressure and that $Ca_{(8)}/Al_{(8)}$ and $Na_{(8)}$ are good indicators of degrees of melting. (5) Our melting model, using primary melts modified by fractionation to MgO = 8.0 wt %, can be applied to natural MORB melts and allows quantitative estimates of parameters of column melting: P_o, P_f, T_o, T_f, and F. (6) Decompression-induced column melting occurs in a thin zone (15–30 km thick) and pinches out away from the EPR axis at 50–60 km. (7) We find lateral temperature differences in the mantle, both along axis and across axis, of 50–60°C over distances of 30–50 km. We ascribe these differences to a weakly conductive thermal profile (versus adiabatic) in the mantle immediately below the lithosphere. If so, these temperature differences can be related to patterns of mantle upwelling. (8) Across-axis melting patterns at the EPR inferred from zero-age seamount MORB melts provide evidence for a wide zone of mantle upwelling due to plate separation. However, the flow may have a central core of higher velocity due to thermal, compositional, and/or melt buoyancy. (9) Along-axis temperature patterns at the EPR suggest a broad region of hot upwelling mantle between Siqueiros and the 11°45'N OSC. Mantle temperature does not correlate with along-axis topography, but it does show a variety of edge effects. These edge effects are not consistent, implying a variety of causes. The EPR is probably supplied principally by a curtain like flow, as suggested by *Lin and Phipps Morgan* [1991]; however, a superimposed hierarchy of local upwelling is probably also present. (10) The MAR at 26°S displays good correlation between topography and melting parameters, including mantle temperature. Deep portions of the MAR, near offsets, have deeper and less extensive melting. This may be partly caused by a focused buoyant upwelling with weaker upwelling below offsets due to a cold edge effect. A variety of other factors may also play a role. (11) The MAR at 26°S exhibits the so-called local trend, which cannot be explained by intracolumn melting alone. We propose that it is due to melting processes resulting from focused buoyant upwelling at slow spreading rates, namely longer melting columns in the center and shorter, deeper columns near offsets.

Acknowledgments. We gratefully acknowledge the following people for their helpful interest and encouragement: J. Sinton, T. Falloon, C. Langmuir, W. White, P. Michael, J. Phipps Morgan, R. Detrick, L. Fleitout, T. Grove, R. Kinzler, J.-G. Schilling, J. Karsten, Y. Chen, J. Lin, W. Su, K. Harpp, and E. Klein. We especially thank T. Falloon and D. Green for providing us with unpublished data and giving some suggestions. The constructive comments of Ridge Summer Institute participants on an early version of this paper are gratefully appreciated, particularly, the extensive, stimulating, and enjoyable discussions with E. Klein, C. Langmuir, J. Phipps Morgan, T. Grove, and R. Kinzler. The first author also thanks J. Sinton, M. Garcia, J. Mahoney, and D. Meunow for their overall help and support. The paper was greatly improved by the comments of C. Langmuir, E. Klein and T. Plank and insightful reviews by B. Bryan, T. Grove, and P. Michael. This work was supported by National Science Foundation grants OCE 89–03296 and OCE–90–00193 and by the Office of Navy Research. University of Hawaii, School of Ocean and Earth Science and Technology contribution 2649.

REFERENCES

Allan, J. F., R. Batiza, M. R. Perfit, D. J. Fornari, and R. O. Sack, Petrology of lavas from the Lamont seamount chain and adjacent Est Pacific Rise, 10°N, *J. Petrol., 30*, 1245–1298, 1989.

Barone, A., and W. B. F. Ryan, Single plume model for asynchronous formation of the Lamont seamount chain and adjacent East Pacific Rise, 10°N, *J. Geophys. Res., 95*, 10,801–10,827, 1990.

Batiza, R., and Y. Niu, Petrology of lavas from the EPR at 9°30'N: Implications for magma chamber processes, *Eos Trans. AGU, 70*, 1399–1400, 1989.

Batiza, R., W. G. Melson, and T. O'Hearn, Simple magma supply geometry inferred beneath a segment of the mid-Atlantic ridge, *Nature, 335*, 428–431, 1988.

Batiza, R., Y. Niu, and W. C. Zayac, Chemistry of seamounts near the East-Pacific Rise: Implications for the geometry of sub-axial mantle flow, *Geology, 18*, 1122–1125, 1990.

Bedard, J. H., Disequilibrium mantle melting, *Earth Planet. Sci. Lett., 91*, 359–366, 1989.

Bender, J. F., C. H. Langmuir, and G. N. Hanson, Petrogenesis of basalt glasses from the Tamayo region, East Pacific Rise, *J. Petrol., 25*, 213–254, 1984.

Bottinga, Y., and C. J. Allègre, partial melting under spreading ridges, *Philos. Trans. R. Soc. London, Ser. A, 288*, 501–525, 1978.

Brodholdt, J. P., and R. Batiza, Global systematics of unaveraged mid-ocean ridge basalt compositions: Comments on "Global correlations of ocean ridge basalt chemistry with axial depth and crustal thickness by E. M. Klein and C. H. Langmuir, " *J. Geophys. Res., 94*, 4231–4239, 1989.

Bryan, W. B., G. Thompson, and J. N. Ludden, Compositional variations in normal MORB from 22°–25°N: mid-Atlantic ridge and Kane Fracture Zone, *J. Geophys. Res., 86*, 11,815–11,836, 1981.

Buck, W. R., and E. M. Parmentier, Convection beneath young oceanic lithosphere: Implication for thermal structure and gravity, *J. Geophys. Res, 91*, 1961–1974, 1986.

Buck, W. R., and W. Su, Focused mantle upwelling below mid-ocean ridges due to feedback between viscosity and melting, *Geophys. Res. Lett., 16*, 641–644, 1989.

Castillo, P. R., and R. Batiza, Mantle dynamics beneath the South Atlantic inferred from the Sr, Nd, and Pb isotope geochemistry of Seamounts, *Nature, 342*, 262–265, 1989.

Crane, K., The spacing of rift axis highs: Dependance on diapiric processes in the underlying asthenosphere, *Earth Planet. Sci. Lett., 72*, 405–415, 1985.

Dick, H. J. B., Abyssal peridotites, very slow spreading ridges and ocean ridge magmatism, In Magmatism in Ocean Basins, edited by A. D. Saunders and M. J. Norry, *Gel. Soc. Special Pub., 42*, 71–106, 1989.

Dick, H. J. B., R. L. Fisher, and W. B. Bryan, Mineralogical variability of

the uppermost mantle along mid-ocean ridges, *Earth Planet. Sci. Lett.*, *69*, 88–106, 1984.

Elthon, D., Pressure of origin of primary mid-ocean ridge basalts, In Magmatism in Ocean Basins, edited by A. D. Saunders and M. J. Norry, *Gel. Soc. Special Pub.*, *42*, 25–136, 1989.

Elthon, D., The petrogenesis of primary mid-ocean ridge basalts, *Rev. Aquat. Sci.*, *2*, 27–53, 1990.

Elthon, D., and C. M. Scarfe, High-pressure phase equilibria of a high-magnesian basalt and the genesis of primary oceanic basalts, *Am. Mineral.*, *69*, 1–15, 1984.

Elthon, D., J. F. Casey, and S. Komor, Mantle chemistry of ultramafic cumulates from the North Arm Mountain Massif of the Bay of Islands ophiolite: Evidence for high-pressure crystal fractionation of oceanic basalts, *J. Geophys. Res.*, *87*, 8717–8734, 1982.

Falloon, T. J., and D. H. Green, Anhydrous partial melting of MORB pyrolite and other peridotite compositions at 10 kbar: Implications for the origin of MORB glasses, *Mineral. Petrol.*, *37*, 181–219, 1987.

Falloon, T. J., and D. H. Green, Anhydrous partial melting of peridotite from 8 to 35kb and the petrogenesis of MORB, *J. Petrol.*, *29*, 379–414, 1988.

Falloon, T. J., D. H. Green, C. J. Hatton, and K. L. Harris, Anhydrous partial melting of a fertile and depleted peridotite from 2 to 30kb and application to basalt petrogenesis, *J. Petrol.*, *29*, 1257–1282, 1988.

Fornari, D. J., M. R. Perfit, J. F. Allan, and R. Batiza, Small-scale heterogeneities in depleted mantle sources: Near-ridge seamount lava geochemistry and implications for mid-ocean-ridge magmatic processes, *Nature*, *331*, 511–513, 1988*a*.

Fornari, D. J., M. R. Perfit, J. F. Allan, R. Batiza, R. Haymon, A. Barone, W. B. F. Ryan, T. Smith, T. Simkin, and M. Luckman, Geochemical and structural studies of the Lamont seamounts : seamounts as indicators of mantle processes, *Earth Planet. Sci. Lett.*, *89*, 63–83, 1988*b*.

Fujii, T., Genesis of mid-ocean ridge basalts, In Magmatism in Ocean Basins, edited by A. D. Saunders and M. J. Norry, *Gel. Soc. Special Pub.*, *42*, 137–146, 1989.

Fujii, T., and H. Bougault, Melting relations of a magnesian abyssal tholeiite and the origin of MORBs, *Earth Planet. Sci. Lett.*, *62*, 283–295, 1983.

Fujii, T., and C. M. Scarfe, Composition of liquids coexisting with spinel lherzolite at 10 kbar and the genesis of MORBs, *Contrib. Mineral. Petrol.*, *90*, 18–28, 1985.

Ghiorso, M. S., and I. S. E. Carmichael, Chemical mass transfer in magmatic processes, II, Application in equilibrium crystallization and assimilation, *Contrib. Mineral. Petrol.*, *90*, 121–141, 1985.

Green, D. H., W. D. Hibberson, and A. L. Jaques, Petrogenesis of mid-ocean ridge basalts. in *The Earth: Its origin, structure, and evolution*, edited by M. W. McElhinney, pp. 265–299. Academic, San Diego, Calif., 1979.

Hanks, T. C., model relating heat flow values near and vertical velocities of mass transport beneath ocean rises, *J. Geophys. Res.*, *76*, 537–544, 1971.

Houseman, G., The deep structure of ocean ridges in a convecting mantle, *Earth Planet. Sci. Lett.*, *64*, 283–294, 1983.

Ito, K., Analytical approach to estimating the source rock of basaltic magmas: Major elements, *J. Geophys. Res.*, *78*, 412–431, 1973.

Jaques, A. L., and D. H. Green, Anhydrous melting of peridotite at 0–15kb pressure and the genesis of tholeiitic basalts, *Contrib. Mineral. Petrol.*, *73*, 287–310, 1980.

Johnson, K., H. B. Dick, and N. Shimizu, Melting in the oceanic upper mantle: An ion microprobe study of diopside in abyssal peridotites, *J. Geophys. Res*, *95*, 2661–2678, 1990.

Klein, E. M., The Clipperton Transform Team, and The CHEPR Team, Geochemistry of basalts collected during Alvin dive within and adjacent to the Clipperton transform fault (10°N, East Pacific Rise), *Eos Trans. AGU*, *68*, 1540, 1987.

Klein E. M. and C. H. Langmuir, Global correlations of ocean ridge basalt chemistry with axial depth and crustal thickness, *J. Geophys. Res.*, *92*, 8089–8115, 1987.

Klein, E. M., and C. H. Langmuir, Local versus global variation in ocean ridge basaltic composition: a reply, *J. Geophys. Res.*, *94*, 4241–4252, 1989.

Langmuir, C. H., and G. N. Hanson, An evaluation of major element heterogeneity in the mantle sources of basalts, *Philos. Trans. R. Soc. London, Ser. A*, *297*, 383–407, 1980*a*.

Langmuir, C. H., and G. N. Hanson, Calculating mineral-melting equilibria with stoichiometry, mass balance, and single-component distribution coefficients, *Adv.Geochem.*, *1*, 247–271, 1980*b*.

Langmuir, C. H., J. F. Bender, A. E. Bence, G. N. Hanson, and S. R. Taylor, petrogenesis of basalts from the FAMOUS area: Mid-Atlantic ridge, *Earth Planet. Sci. Lett.*, *36*, 133–156, 1977.

Langmuir, C. H., J. F. Bender, and R. Batiza, Petrological and tectonic segmentation of the East Pacific Rise, 5°30'–14°30', *Nature*, *322*, 422–429, 1986.

Lin, J., and J. Phipps Morgan, The spreading rate dependance of three-dimensional mid-ocean ridge gravity structure, *Geophys. Res. Lett.*, in press, 1991.

Lin, J., G. M. Purdy, H. Schouten, J.-C. Sempere, and C. Zervas, Evidence from gravity data for focused magmatic accretion along the mid-Atlantic ridge, *Nature*, *344*, 627–632, 1990.

Maaløe, S., Geochemical aspects of permeability controlled partial melting and fractional crystallization, *Geochim. Cosmochim. Acta*, *46*, 43–57, 1982.

Macdonald, K. C., J. C. Sempere, P. J. Fox, and R. Tyce, Tectonic evolution of ridge axis discontinuities by the meeting, liking and self-decapitation of neighboring ridge segments, *Geology*, *15*, 993–997, 1987.

Macdonald, K. C., P. J. Fox, L. J. Perram, M. F. Eisen, R. M. Haymon, S. P. Miller, S. M. Carbote, M.-H. Cormier, and A. N. Shor, A new view of the mid-ocean ridge from the behavior of ridge axis discontinuities, *Nature*, *335*, 217–225, 1988.

McKenzie, D., The generation and compaction of partially molten rock, *J. Petrol.*, *25*, 713–765, 1984.

McKenzie, D., ^{230}Th - ^{238}U disequilibrium and the melting processes beneath ridge axes, *Earth Planet. Sci. Lett.*, *72*, 137–152, 1985*a*.

McKenzie, D., The extraction of magma from the crust and mantle, *Earth Planet. Sci. Lett.*, *79*, 81–91, 1985*b*.

McKenzie, D., and M. J. Bickle, The volume and composition of melt generated by extension of the lithosphere, *J. Petrol.*, *29*, 625–679, 1988.

Natland, J. H., Partial melting of a lithologically heterogeneous mantle: inferences from crystallization histories of magnesian abyssal tholeiites from the Siqueiros Fracture Zone, in Magmatism in Ocean Basins, edited by A. D. Saunders and M. J. Norry, *Gel. Soc. Special Pub.*, *42*, 41–70, 1989.

Nicolas, A, A melt extraction model based on structural studies in mantle peridotites, *J. Petrol.*, *27*, 999–1022, 1986.

Nicolas, A, Structures of ophiolites and dynamics of oceanic lithosphere, 368pp., *Kluwer Academic*, Dordrecht, pp 368, 1989.

Nielsen, R. L., A method for the elimination of the compositional dependence of trace element distribution coefficients, *Geochim. Cosmochim. Acta*, *49*, 1775–1779, 1985.

Nielsen, R. L., A method for the simulation of combined major and trace element liquid line of descent, *Geochim. Cosmochim. Acta*, *52*, 27–38, 1988.

Nielsen, R. L., and M. A. Dungan, Low pressure mineral-melt equilibria in natural anhydrous mafic system, *Contrib. Mineral. Petrol.*, *84*, 310–326, 1983.

Niu, Y., and R. Batiza, Chemistry of near-EPR seamounts chains: Implications for magma supply process, *Eos Trans. AGU*, *70*, 1400, 1989.

Niu, Y., and R. Batiza, DENSCAL: A program for calculating densities of silicate melts and mantle minerals in melting range, *Comput.Geosci.*, *17*, 679–687, 1991.

O'Hara, M. J., Primary magmas and the origin of basalts, *Scott. J. Geol.*, *1*, 19–40, 1968.

Oxburgh, E. R., and D. L., Turcotte, Mid-ocean-ridge and geotherm distribution during mantle convection: *J. Geophys. Res.*, *73*, 26–43, 1968.

Phipps Morgan, J., Melt migration beneath mid-ocean ridge spreading centers, *Geophys. Res. Lett.*, *14*, 1238–1241, 1987.

Phipps Morgan, J., and D. W. Forsyth, Three-dimensional flow and temperature perturbations due to a transform offset: Effects on oceanic crustal upper mantle structure, *J. Geophys. Res*, *93*, 2955–2966, 1988.

Presnall, D. C., and J. D. Hoover, Composition and depth of origin of primary mid-ocean ridge basalts, *Contrib. Mineral. Petrol.*, *87*, 170–178, 1984.

Rabinowicz, M., G. Ceuleneer, and A. Nicolas, Melt segregation and flow in mantle diapirs below spreading centers: Evidence from Oman ophiolite, *J. Geophys. Res*, *92*, 3475–3486, 1987.

Ribe, N. M., Theory of melt segregation — a review, *J. Volc. Geotherm. Res.*, *33*, 241–253, 1987.

Ribe, N. M., On the dynamics of mid-ocean ridges, *J. Geophys. Res*, *93*, 429–436, 1988.

Richter, F. M., and D. McKenzie, Dynamic models for melt segregation from a deformable matrix, *J. Geol.*, *92*, 729–740, 1984.

Riley, G. N., and D. L. Kohlstedt, an experimental study of melt migration in an olivine-melt system, in *Magma Transport and Storage*, edited by M. P. Ryan, John Wiley, New York, in press, 1990

Rubin, K. H., and J. D. Macdougall, ^{226}Ra excesses in mid-ocean ridge basalts and mantle melting, *Nature*, *225*, 149–157., 1985.

Schouten, H., H. J. B. Dick and K. D. Klitgord, Segmentation of mid-ocean ridges, *Nature*, *317*, 225–229, 1985.

Scott, D. R., and Stevenson, D. J., A self-consistent model of melting, magma migration and buoyancy-driven circulation beneath mid-ocean ridges, *J. Geophys. Res.*, *94*, 2973–2988, 1989.

Shaw, D. M., Trace element fractionation during anatexs, *Geochim. Cosmochim. Acta*, *34*, 237–243, 1970.

Sinton, J. M., S. M. Smaglik, J. J. Mahoney, and K. C. Macdonald, Magmatic processes at superfast spreading ridges: Glass compositional variations along the EPR 13° – 23°S, *J. Geophys. Res.*, *96*, 6133–6155, 1991.

Sleep, N. H., Tapping of melts by veins and dikes, *J. Geophys. Res. 93*, 10,255–10,272, 1988.

Smith, T., and R. Batiza, New field and laboratory evidence for the origin of hyaloclastite flows on seamounts, *Bull. Volcanol.*, *57*, 96–114, 1989.

Sotin, C., and E. M. Parmentier, Dynamic consequences of compositional and thermal density stratification beneath spreading centers, *Geophys. Res. Lett.*, *16*, 835–838, 1989.

Spiegelman, M., and D. McKenzie, Simple 2-D models for melt extraction at mid-ocean ridges and island arcs, *Earth Planet. Sci. Lett.*, *83*, 137–152, 1987.

Stolper, E., A phase diagram for mid-ocean ridge basalts: Preliminary results and implications for petrogenesis, *Contrib. Mineral. Petrol.*, *74*, 13–27, 1980.

Tighe, S., (Ed.), *East Pacific Rise Data Synthesis*, Joint Oceanographic Institute, Washington, D. C., 1988.

Walker, D., T. Shibata, and S. E. DeLong, Abyssal tholeiites from the Oceanographer Fracture Zone, II, Phase equilibria and mixing, *Contrib. Mineral. Petrol.*, *70*, 111–125, 1979.

Weaver, J. S., and C. H. Langmuir, Calculation of phase equilibrium in mineral-melt systems, *Comput. Geosci.*, *16*, 1–19, 1990.

Whitehead, J. A., Jr., H. J. B. Dick, and H. Schouten, A mechanism for magmatic accretion under spreading centers, *Nature*, *312*, 146–148, 1984.

Williams, R. W., and J. B. Gill, Effects of partial melting on the uranium decay series, *Geochim. Cosmochim. Acta*, *53*, 1607–1619, 1989.

Yoder, H. S., *Generation of Basaltic Magma*, 265 pp.,National Academy of Science Press, Washington, D. C., 1976.

R. Batiza and Y. Niu, Department of Geology and Geophysics, University of Hawaii at Manoa, Honolulu, Hawaii, 96822.

(Received March 14, 1991;
revised July 1, 1991;
accepted July 18, 1991.)